Geochemistry, Geophysics, Geosystems®

AGU ADVANCING EARTH AND SPACE SCIENCES

RESEARCH ARTICLE
10.1029/2023GC011088

Special Section:
Frontiers in lithospheric dynamics: Bridging scales through observations, experiments, and computations

A Cascadia Slab Model From Receiver Functions

Wasja Bloch[1], Michael G. Bostock[1], and Pascal Audet[2]

[1]The University of British Columbia, Vancouver, BC, Canada, [2]University of Ottawa, Ottawa, ON, Canada

Abstract We map the characteristic signature of the subducting Juan de Fuca and Gorda plates along the entire Cascadia forearc from northern Vancouver Island, Canada, to Cape Mendocino in northern California, USA, using teleseismic receiver functions. The subducting oceanic crustal complex, possibly including subcreted material, is parameterized by three horizons capable of generating mode-converted waves: a negative velocity contrast at the top of a low velocity zone underlain by two horizons representing positive contrasts. The amplitude of the conversions varies likely due to differences in composition and/or fluid content. We analyzed the slab signature for 298 long-running land seismic stations, estimated the depth of the three interfaces through inverse modeling and fitted regularized spline surfaces through the station control points to construct a margin-wide, double-layered slab model. Crystalline terranes that act as the static backstop appear to form the major structural barrier that controls the slab morphology. Where the backstop recedes landward beneath the Olympic Peninsula and Cape Mendocino, the slab subducts sub-horizontally, while the seaward-protruding and thickened Siletz terrane beneath central Oregon causes steepening of the slab. A tight bend in slab morphology south of the Olympic Peninsula coincides with the location of recurring large intermediate depth earthquakes. The top-to-Moho thickness of the slab generally exceeds the thickness of the oceanic crust by 2–12 km, suggesting thickening of the slab or underplating of slab material to the overriding North American plate.

Plain Language Summary The tectonic Juan de Fuca plate, that underlies the easternmost North Pacific Ocean off-shore Vancouver Island, Washington, Oregon, and northern California, is being pushed beneath the North American continent by plate tectonics. On its way deep into the Earth, the plate deforms. In this study, we analyze seismograms of distant earthquakes which were recorded within the study area. Through signal and data processing, we decipher information about the location, orientation, and properties of the down-going oceanic plate beneath the continent. The data show that the plate protrudes shallowly dipping under the continent beneath the Olympic Peninsula (Washington) and Cape Mendocino (California), while it dips down more steeply under central Oregon and Vancouver Island (British Columbia). This configuration suggests that Siletzia, an old and rigid basalt plateau that forms the central part of the study area, controls the shape of the down-going plate. Furthermore, the oceanic plate appears to significantly thicken at depth, which may indicate that parts of it accumulate at the base of the continent. These results are important to better understand the subduction process and may help to infer the location of the deeper extent of rupture in a future potential strong earthquake.

Key Points:

- We model Cascadia subduction stratigraphy as three dipping horizons
- Slab morphology is controlled by crystalline terrane backstops
- A near-ubiquitous ~2–10 km thick ultralow velocity zone in the tremor zone correlates with the E-layer

Supporting Information:

Supporting Information may be found in the online version of this article.

Correspondence to:

W. Bloch,
wasja@wasjabloch.de

Citation:

Bloch, W., Bostock, M. G., & Audet, P. (2023). A Cascadia slab model from receiver functions. *Geochemistry, Geophysics, Geosystems*, *24*, e2023GC011088. https://doi.org/10.1029/2023GC011088

Received 12 JUN 2023
Accepted 2 OCT 2023

Author Contributions:

Conceptualization: Wasja Bloch, Michael G. Bostock
Data curation: Wasja Bloch
Formal analysis: Wasja Bloch
Funding acquisition: Wasja Bloch
Investigation: Wasja Bloch
Methodology: Wasja Bloch, Michael G. Bostock, Pascal Audet
Software: Wasja Bloch, Michael G. Bostock, Pascal Audet
Supervision: Michael G. Bostock

1. Introduction

The boundary between the down-going oceanic and overriding continental plates in subduction zones is the locus of major seismic moment release in great earthquakes and enigmatic slow earthquakes. Knowledge about its location and characteristics is key to understanding seismogenesis, tsunamigenesis, and geodynamic processes taking place in subduction zones. During the subduction process, the down-going slab is subject to mechanical and chemical alterations, including flexure, shearing, increases in temperature and pressure, metamorphism, fluid generation and redistribution, metasomatism, and other complex geodynamical processes. All of these factors are expected to influence the slab's mechanical behavior.

In the Cascadia subduction zone, the Juan de Fuca plate (JdF) subducts beneath the North American plate at velocities that vary between 42 mm yr^{-1} at its northern end near the Nootka Fault Zone, to 36 mm yr^{-1} at its southern end near the Blanco Fracture Zone. The plate subducts at an azimuth of ~N56°E. To the south, the Gorda micro-plate subducts at 33 mm yr^{-1} with an azimuth of N52°E (DeMets et al., 1994). The Explorer plate to the north does not subduct but more likely underthrusts the North American Plate beneath northern Vancouver Island (Audet et al., 2008; Merrill et al., 2022; Riddihough, 1984; Savard et al., 2020). To the north, the

Validation: Wasja Bloch
Visualization: Wasja Bloch
Writing – original draft: Wasja Bloch
Writing – review & editing: Wasja Bloch, Michael G. Bostock, Pascal Audet

subduction system transforms into the right-lateral Queen Charlotte and Revere-Dellwood Faults and to the south into the San Andreas Fault (Figure 1).

Immediately landward of the deformation front, the subduction interface can be identified in high-frequency reflection seismic sections along the entire Cascadia margin (e.g., Calvert, 1996; Calvert & Clowes, 1991; Carbotte et al., 2022; Clowes et al., 1987b; Flueh et al., 1998; Gulick et al., 1998; Han et al., 2016; MacKay et al., 1992). In places, the structural décollement is located within the lower part of the sedimentary blanket, implying sediment subduction (Flueh et al., 1998; Han et al., 2016; Tréhu et al., 1994, 2012).

Farther downdip, the JdF has been identified below the Salish Sea on marine seismic sounding transects through the Juan de Fuca Strait and Georgia Strait. At about 20 km depth, the sharp <2 km thick reflector that marks the top of the slab widens into an up to 10 km wide reflection band, the so-called E-layer (e.g., Clowes et al., 1987a; Nedimović et al., 2003), that extends to depths of at least ∼50 km (Calvert et al., 2006). A similarly thick reflective zone has been identified atop the subducting JdF at 35–40 km depth beneath central Oregon (Keach et al., 1989; Tréhu et al., 1994). It has been argued that the E-layer represents the transition into a wider shear zone that creeps aseismically and hosts episodic tremor and slip (ETS, see e.g., Calvert et al., 2020; Nedimović et al., 2009).

At lower frequencies (≤1 Hz), the receiver function method can be used to image sharp velocity changes such as the Moho or the Conrad interface, low-velocity zones, and mantle transition zone discontinuities. It has previously been employed to identify discontinuities in complex 3-D geological structures worldwide for example, in the Himalayan belt (e.g., Caldwell et al., 2013; Singer et al., 2017; Subedi et al., 2018; Xu et al., 2021), the Alps (e.g., Colavitti et al., 2022; Liu et al., 2022; Michailos et al., 2023), the Andes (e.g., Bar et al., 2019; Rodriguez & Russo, 2019; Yuan et al., 2000), and Japan (e.g., Chen et al., 2005; Li et al., 2000; Niu et al., 2005).

In Cascadia, the subduction zone stratigraphy has also been previously characterized using teleseismic *P*-wave receiver function data (e.g., Abers et al., 2009; Bostock et al., 2002; Cassidy & Ellis, 1993; Langston & Blum, 1977; Mann et al., 2019; McGary et al., 2014; Nabelek et al., 1993; Nicholson et al., 2005). A recent study employing receiver functions, local tomography and seismic reflection data in southern Vancouver Island suggests that the oceanic crust may reside below the E-layer (Calvert et al., 2020) and that at least part of the E-layer comprises an ultralow *S*-wave velocity zone (ULVZ), with V_P/V_S of the order of 2–3 (Audet et al., 2009; Cassidy & Ellis, 1993). In local seismic tomograms, the slab stratigraphy oftentimes appears smeared into a single layer with moderately elevated V_P/V_S in the order of 1.8–2.0, consistent with basaltic or gabbroic lithologies with some contribution of fluid-filled pores. Interpretation of the oceanic Moho in tomographic models is less ambiguous, where it appears as a strong negative V_P/V_S gradient to values lower than 1.7 that mark the oceanic mantle below (Guo et al., 2021; Merrill et al., 2020, 2022; Savard et al., 2018).

An initial margin-wide map of the top of the JdF was constructed from a mixed data set of earthquake hypocenters, active source seismic profiles, receiver functions and local earthquake tomograms with the aim to model interseismic strain accumulation in the overriding plate (Flück et al., 1997). With increasing data availability over time and a better understanding of subduction processes, the initial model has been updated and extended in space using additional constraints from seafloor magnetic anomalies, deeper seismicity and diffraction of strong earthquake first arrivals (McCrory et al., 2004) and later from relocated earthquake hypocenters and electrical conductivity profiles (Hayes et al., 2018; McCrory et al., 2012). Other slab models are based purely on receiver functions (Audet et al., 2010; Hansen et al., 2012).

Despite a broad agreement in recovered slab depths to within ∼10 km, considerable differences exist across these models. These differences are associated with data uncertainties, the fact that the slab models are based on different data types, and with ambiguities in the interpretation of proxies for what constitutes the "slab top" (McCrory et al., 2012).

Here, we construct a margin-wide slab model that honors an oceanic crustal stratigraphy that may consist of up to two layers, including the possibility of subcreted material. Our model is based on the observation that receiver function images of the slab exhibit characteristic successions of positively and negatively polarized conversions that can be explained by interfering forward- and back-scattered seismic wave modes originating at three interfaces. We map these interfaces continuously along dip from the coast to the forearc lowlands (Salish Sea, Willamette Valley) and along strike from Brooks Peninsula on northern Vancouver Island, Canada, to Cape Mendocino, USA (Figure 1). Our results demonstrate how the overall slab morphology is controlled by the

10.1029/2023GC011088

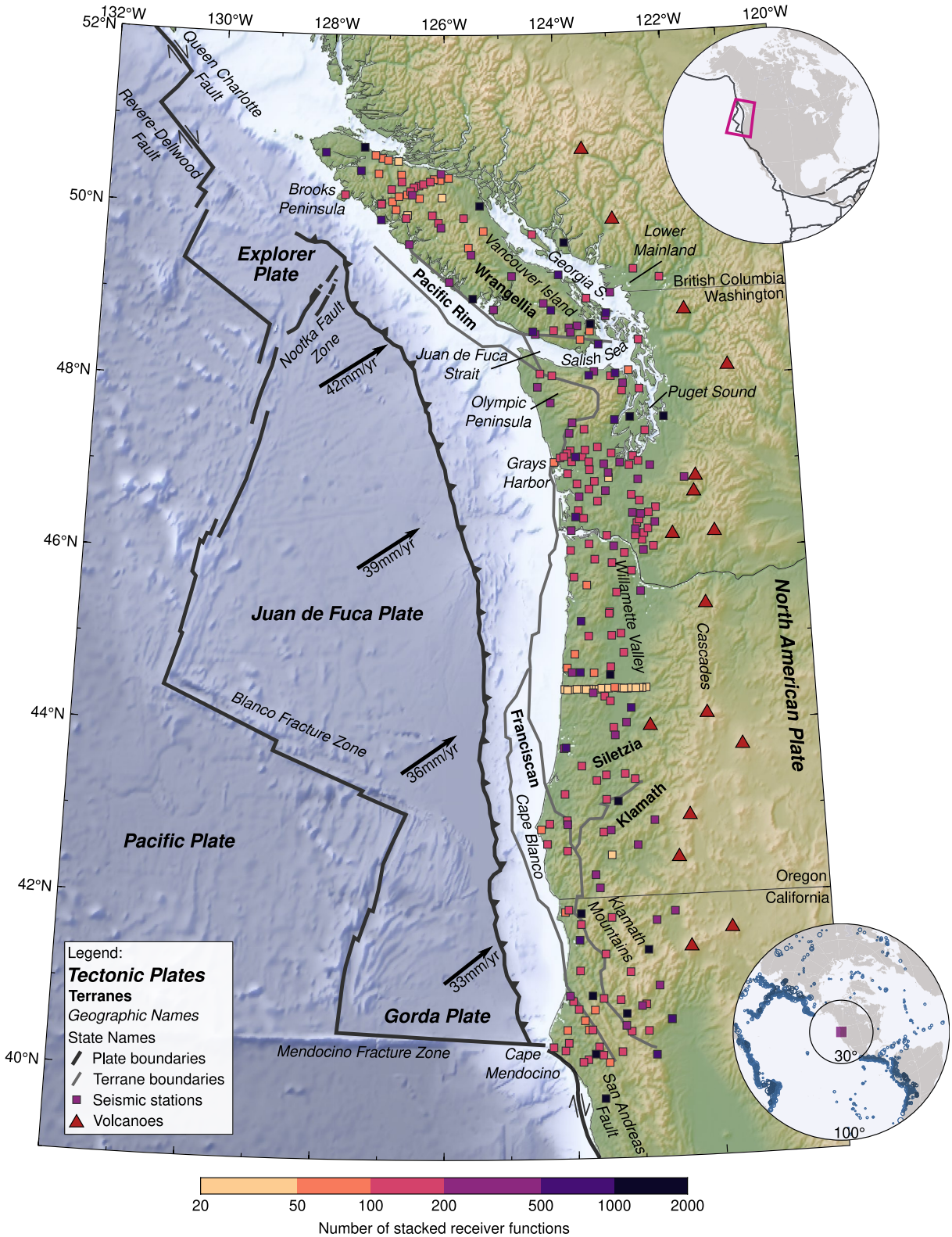

Figure 1. The tectonic setting of the Cascadia subduction zone and station distribution employed to determine the slab geometry under the forearc. The convergence of the Juan de Fuca and Gorda Plates relative to stable North America is shown as arrows (DeMets et al., 1994). Terrane boundaries modified after Watt and Brothers (2020). Top inset: Location of the study area on the North American continent. Bottom inset: Earthquake source distribution form 30° to 100° epicentral distance used to compute receiver functions.

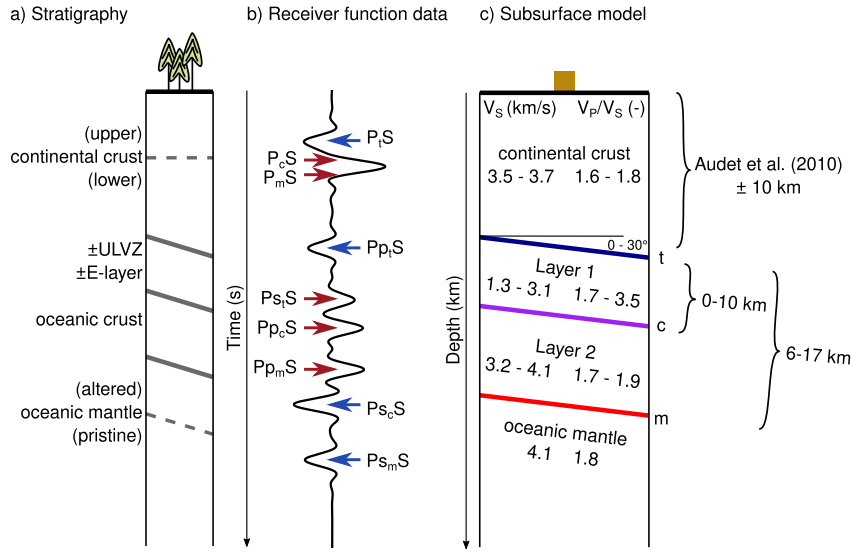

Figure 2. (a) Forearc stratigraphy with the previously identified interfaces. (b) Schematic radial receiver function with the forward and back scattered mode conversions used to constrain the model. Phases may interfere and cancel out in some cases. The absence of specific phase combinations may therefore be meaningful. Upper case letters indicate upgoing rays, lower case letters down-going rays, and subscript the scattering interface. (c) Parameterization of the subsurface model. The possible presence of additional interfaces complicates the phase associations.

location of the static backstop. A subduction stratigraphy that is generally thicker than the incoming oceanic crust is testament to complex deformation processes affecting slab morphology along the subduction trajectory.

2. Data and Methods

A total of 45,601 individual receiver functions recorded at 298 seismic stations distributed across the Cascadia forearc contributed to the slab model. For each station, 100 s recordings symmetric about the *P*-wave arrival (i.e., 50 s noise and 50 s signal, for convenience) of earthquakes with magnitudes between 5.5 and 8, in the distance range between 30° and 100°, were downloaded (Figure 1). Waveforms with a signal-to-noise ratio smaller than 5 dB on the vertical component or 0 dB on the radial component were excluded. The instrument responses were removed and the seismograms were transformed into the upgoing *P-SH-SV* modes (Kennett, 1991). The *P*-component was trimmed to the time window beyond which the envelope fell below 2% of the maximum amplitude and a cosine taper was applied.

2.1. Receiver Function Processing

The three-component *P*-wave spectra were scaled by their signal-to-noise ratio and binned according to their incidence angle in back azimuth bins of 7.5° and horizontal slowness bins of 0.002 s km^{-1}. Within each bin, radial and transverse receiver functions were computed through frequency domain simultaneous deconvolution (Gurrola et al., 1995), with an optimal damping factor found through generalized cross validation (Bostock, 1998). This approach mitigates the instabilities inherent in spectral division by stacking spectra prior to deconvolution.

2.2. Parameter Search

The continental forearc and subducting slab were parameterized as three layers over a mantle half-space, with the subduction stratigraphy bounding interfaces labeled as *t* (top), *c* (central), and *m* (Moho) (Figure 2). Synthetic receiver functions were calculated through ray-theoretical modeling of plane-wave scattering at the model interfaces (Bloch & Audet, 2023; Frederiksen & Bostock, 2000; Figure 2b). The thickness, *S*-wave velocity (V_S) and *P*- to *S*-wave velocity ratio (V_P/V_S) of each layer, as well as the common strike and dip of the bottom two layers and the top of the half space (in total 11 parameters), were optimized simultaneously through a simulated annealing global parameter search scheme (Xiang et al., 1997), as implemented in the *SciPy* package (Virtanen

et al., 2020). In analogy to the annealing process in metallurgy, the scheme samples the misfit function stochastically under a decreasing "temperature" that gradually favors low-misfit parameter combinations. In this way, the algorithm can escape local minima in the misfit function. It has proven efficient in converging toward the global minimum in problems with many independent variables (Kirkpatrick et al., 1983). The misfit was defined as the anti-correlation (1 minus the cross correlation coefficient) between the observed and predicted receiver functions, bandpass filtered between 2 and 20 s period duration.

Initial thickness bounds for the continental crust (Figure 2c) were based on the slab model of Audet et al. (2010) (±10 km). Maximum Layer 1 thickness was constrained by the maximum E-layer thickness of 10 km (Nedimović et al., 2003) and maximum Layer 2 thickness with the thickness of the incoming oceanic crust of 6.5 km (Han et al., 2016). Layer 1 could attain zero-thickness if the E-layer were absent. Because the igneous oceanic crust may be part of the E-layer, Layers 1 and 2 were constrained to have a combined minimum thickness of 6 km. Velocity bounds (Figure 2c) for the continental crust and Layer 2 were based on the 2σ interval of the expected lithologies for continental and oceanic crust, respectively, from the seismic velocity database of Christensen (1996); and for Layer 1 on an analytic poro-elastic model (Bloch et al., 2018) constrained to match the V_P/V_S observations of the ULVZ (Audet et al., 2009).

To verify convergence toward a global minimum, the global parameter search was initialized with at least three different random number seeds, which affect the distribution from which trial parameter estimates are drawn. The resulting data predictions and models were checked for consistency with neighboring stations, previous tomographic profiles (Guo et al., 2021; Kan et al., 2023; Merrill et al., 2020; Savard et al., 2018), hypocentral locations of low-frequency earthquakes (LFEs) within tremor (Armbruster et al., 2014; Plourde et al., 2015; Royer & Bostock, 2014; Savard et al., 2018, 2020) and offshore marine seismic profiles (Suzanne Carbotte, pers. comm; Carbotte et al., 2023). If none of the minimum misfit models of an individual station were consistent with the above constraints, the global search was repeated within narrower bounds around a preferred solution from a neighboring reliable station. Such a model was used only in case it converged toward values away from thickness bounds (Figure 3). For each of the three horizons, a quality and a nominal depth uncertainty were assigned. Quality *A* denotes a horizon where at least one back-scattered phase in the predicted data correlates with the observed data (Figures 3a and 3b), the predicted data are consistent among neighboring stations and the modeled horizon depth is consistent with the available external constraints. A quality *B* horizon shows a good phase correlation, but the predicted data are inconsistent with neighboring stations and/or the modeled depth is inconsistent with external constraints. Quality *C* was assigned to horizons that do not show a convincing correlation between observed and predicted data, usually due to data with low signal-to-noise levels. Stations above the forearc lowlands for which the characteristic slab signature (Figure 2b) is decisively absent and where the onset of eclogitization is expected were marked with a quality *X*. The nominal depth uncertainty was estimated from the scatter of the local minima in the vicinity of the preferred minimum, as determined in the global search (Figure 3c).

2.3. Fitting of Interfaces

In total, 171, 143 and 137 quality *A* nodes were determined to constrain the *t*, *c* and *m* interfaces, respectively. At the trench, 105 nodes at 3 km below the local bathymetry were inserted to constrain the *t* and *c* interfaces, and at 6.5 km deeper to constrain the *m* interface, representing typical sediment and igneous crustal thicknesses (Han et al., 2016). A spline surface (Sandwell, 1987) was fitted to these nodes to yield margin-wide depth models. The spline coefficients were found using singular value decomposition (Aster et al., 2018; Wessel & Becker, 2008), with the nominal depth uncertainties supplied as weights. The solution was damped by retaining the 116, 117, and 116 largest singular values for the *t*, *c*, and *m* interfaces, respectively, based on the analysis of L-curves and the Akaike information criterion (Figure S1 in Supporting Information S1).

3. Results

3.1. Margin-Scale Slab Morphology

The signature of the subduction stratigraphy can be traced along the forearc from Brooks Peninsula on northern Vancouver Island, across Vancouver Island, the Olympic Peninsula, the Willamette Valley in Washington and Oregon, into the Klamath Mountains and to Cape Mendocino in northern California (Figures S2–S50 in Supporting Information S1). The recovered velocities of the three model layers are consistent for neighboring

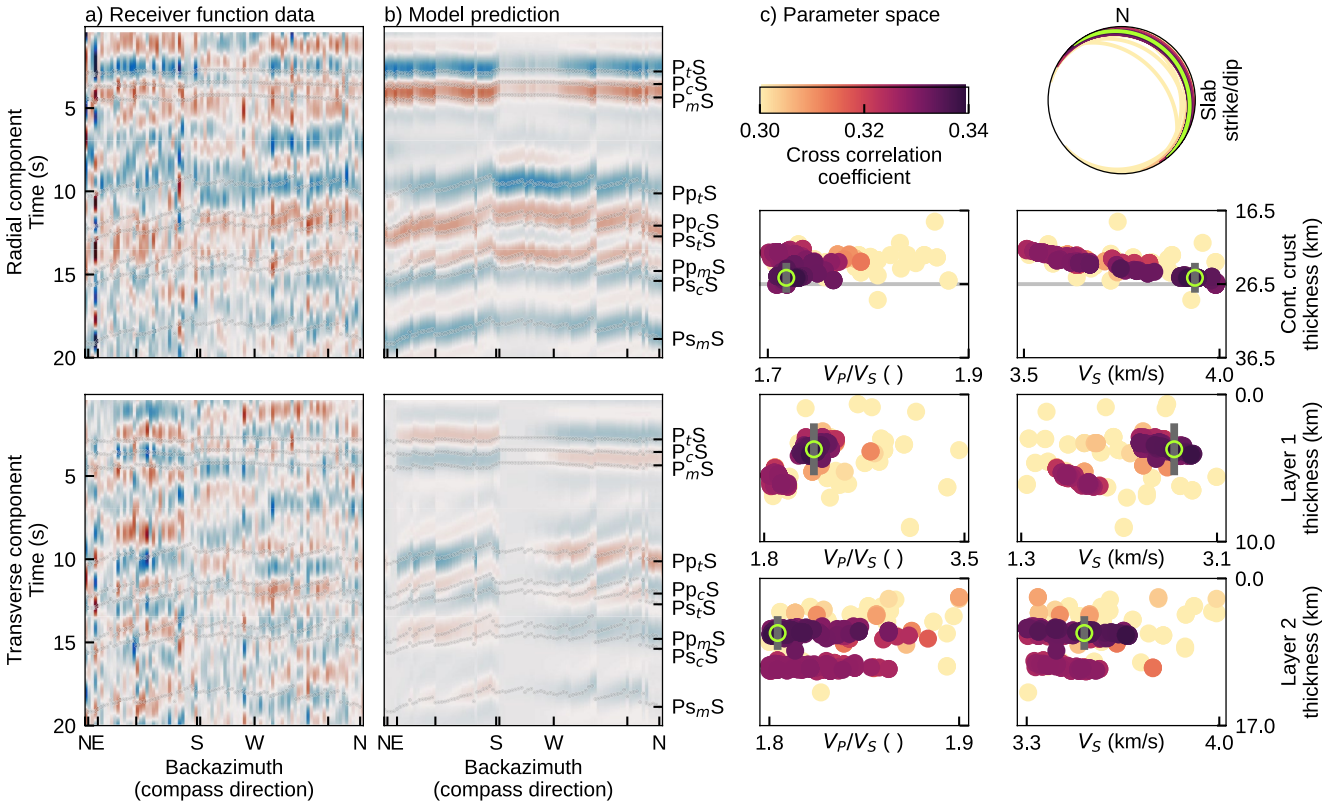

Figure 3. Global search for subsurface parameters. (a) Receiver function data for station C8.TWBB. (b) Predicted data from the best fitting model with phase labels as in Figure 2b. (c) Local minima encountered in the global search for the 11 subsurface parameters (thickness against V_P/V_S in the left column and against V_S in the right column) using a simulated annealing scheme with the preferred solution marked with a green circle and nominal depth uncertainties with a gray bar. Note the presence of a local minimum. If such minimum proved more consistent with external constraints and neighboring stations, the global search was repeated within bounds around that minimum.

stations (Figure S51 in Supporting Information S1). Slab morphology suggests a division into four segments: the Klamath, Central, Olympic and Vancouver Island segments (Figure 4).

The Central segment, between 44° and 47°N, reveals the steepest dip, between 10° and 20°, and overall deepest slab, with the *t* horizon located between 15 and 25 km depth along the coast and dipping to 35–45 km depth before losing expression in advance of the volcanic arc. The Central segment is flanked to the north and south by flatter segments. In the south, the Klamath segment, located between ~40° and 44°N, displays a more shallowly dipping slab, a contorted *t* horizon beneath Cape Mendocino and a contorted *m* horizon along the landward projection of the Blanco Fracture zone. The Olympic segment, located between 47° and 49°N, exhibits a shallow dipping (0–5°) slab beneath the coastal region, and is delimited to the south by a steep downward bend in the *t* and *m* horizons near Grays Harbor and by a bend in the slab strike just north of the Juan de Fuca Strait. Along the dip, the slab steepens as it approaches Puget Sound, where it begins to lose expression (Abers et al., 2009). The northernmost Vancouver Island segment is characterized by a moderately dipping slab. Near the northern terminus of subduction, north of Nootka Island, the *t* and *c* conversions appear disturbed. In summary, from north to south, the slab (a) dips gently and steepens down dip under Vancouver Island, (b) dips shallowly beneath the Olympic Peninsula, (c) steepens significantly beneath the Oregon Coastal Mountains, (d) subducts in a step-like fashion in front of Klamath Mountains, and (e) becomes contorted in the Cape Mendocino area. A comparison with previous slab models is shown in Figure S52 in Supporting Information S1.

3.2. Regional Scale

3.2.1. Central Segment

Across the Central segment, the slab has been imaged with seismological methods using data from the CASC'93 experiment that comprised a temporary broadband array of ~30 stations deployed across the Oregon

10.1029/2023GC011088

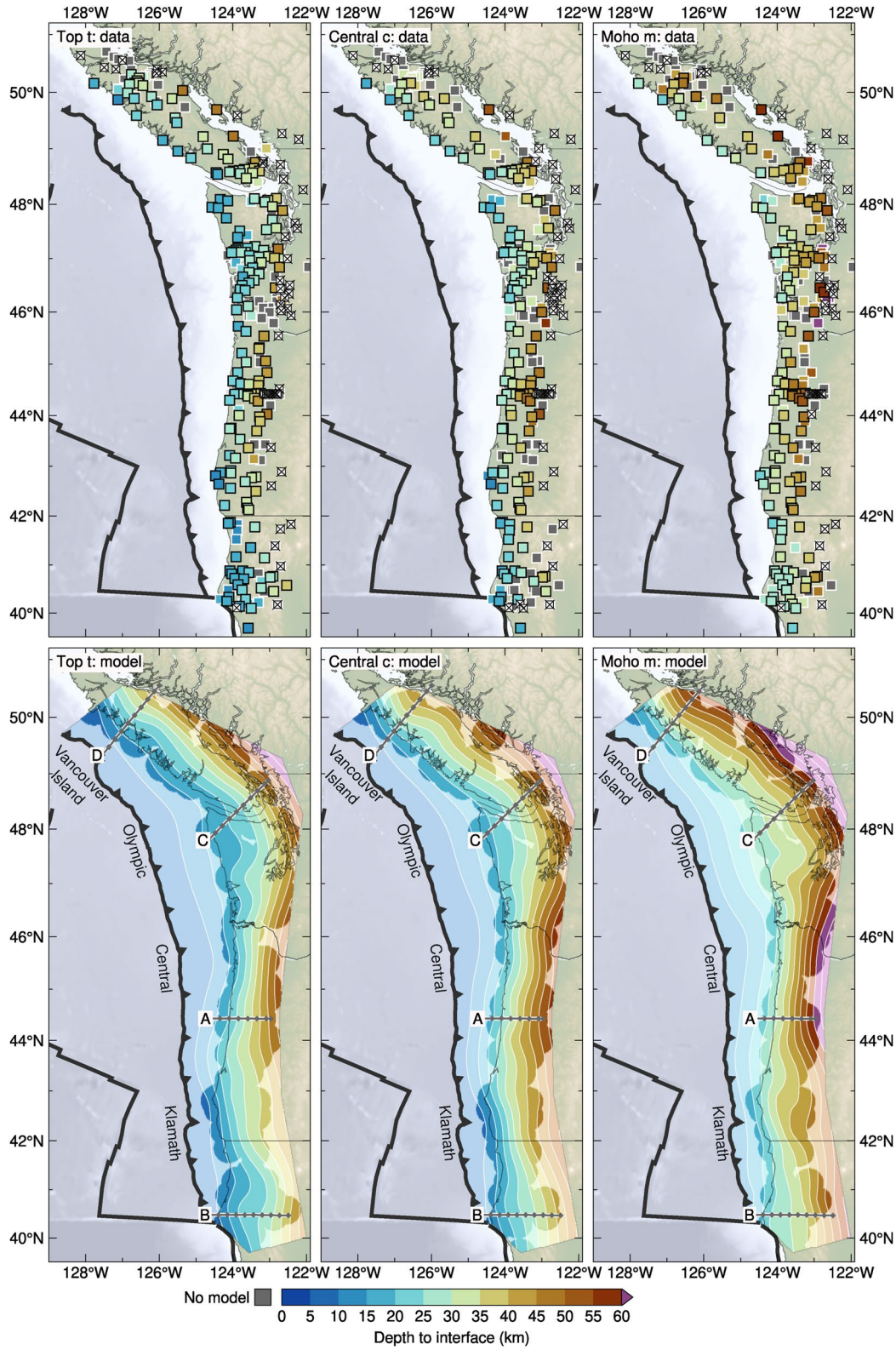

Figure 4. Depth to the *t*, *c*, and *m* horizons. Top row: Data points by quality (black frames: *A*; white frames: *B*; not used for fitting the interface; and grayed out: *C*). Stations marked *X* do not show the respective interface and are interpreted as the location of the eclogitization front. Bottom row: modeled interfaces (Section 2.3) and profile locations (Figures 5–8).

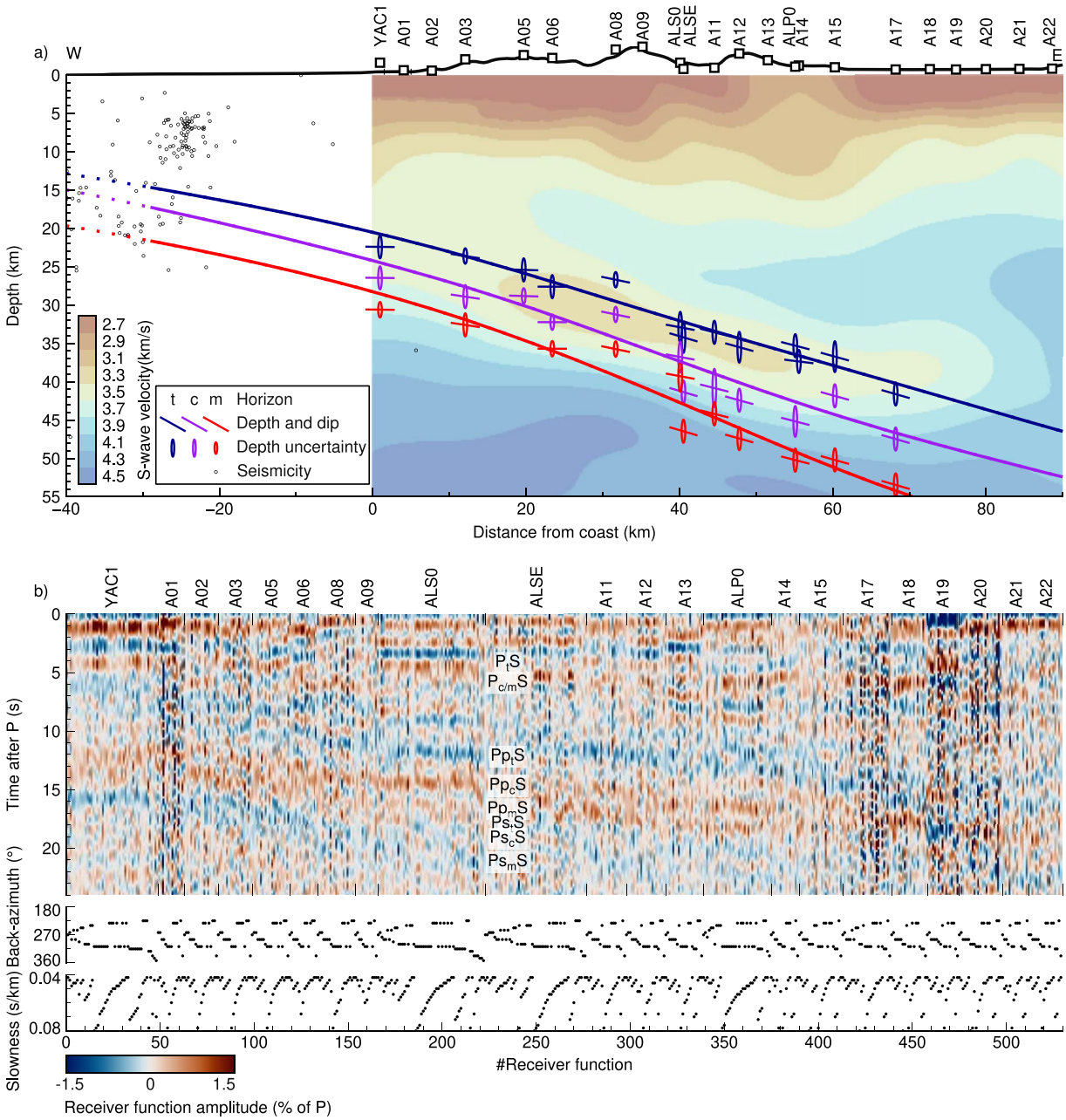

Figure 5. (a) Profile A (Figure 4) with slab model and control points superimposed on the V_S model of Kan et al. (2023) with seismicity from Morton et al. (2023). Comparison with the V_P/V_S image is shown in Figure S53 in Supporting Information S1. (b) Receiver function sections of individual stations sorted along the profile, with the receiver functions within each section sorted by the angular distance of the ray back azimuth from the profile azimuth (90°). 1.5–20 s bandpass filter was applied. Phase labels correspond as in Figure 2.

forearc (Nabelek et al., 1993). It yielded the first dense receiver function studies targeting the subduction zone structure that clearly revealed subducting oceanic crust (Bostock et al., 2002; Rondenay et al., 2001; Tauzin et al., 2016). The comparison of our model with the teleseismic full-waveform tomogram of Kan et al. (2023) yields a consistent picture of the subduction stratigraphy (Figure 5). As in previous studies, Kan et al. (2023) image the subducting Juan de Fuca plate as a distinctive low-V_S zone, which attains velocities as low as 3.3 km s^{-1}. All three horizons parallel this structure, with *t* marking the top of the LVZ and *c* and *m* marking two steps in the gradual increase toward high V_S, characteristic for oceanic mantle of the order of 4.3 km s^{-1}. This structure has a very clear and characteristic expression in the receiver functions, which weakens near station XZ.A18, beneath the Willamette Valley, as in the tomogram. The entire stratigraphic sequence

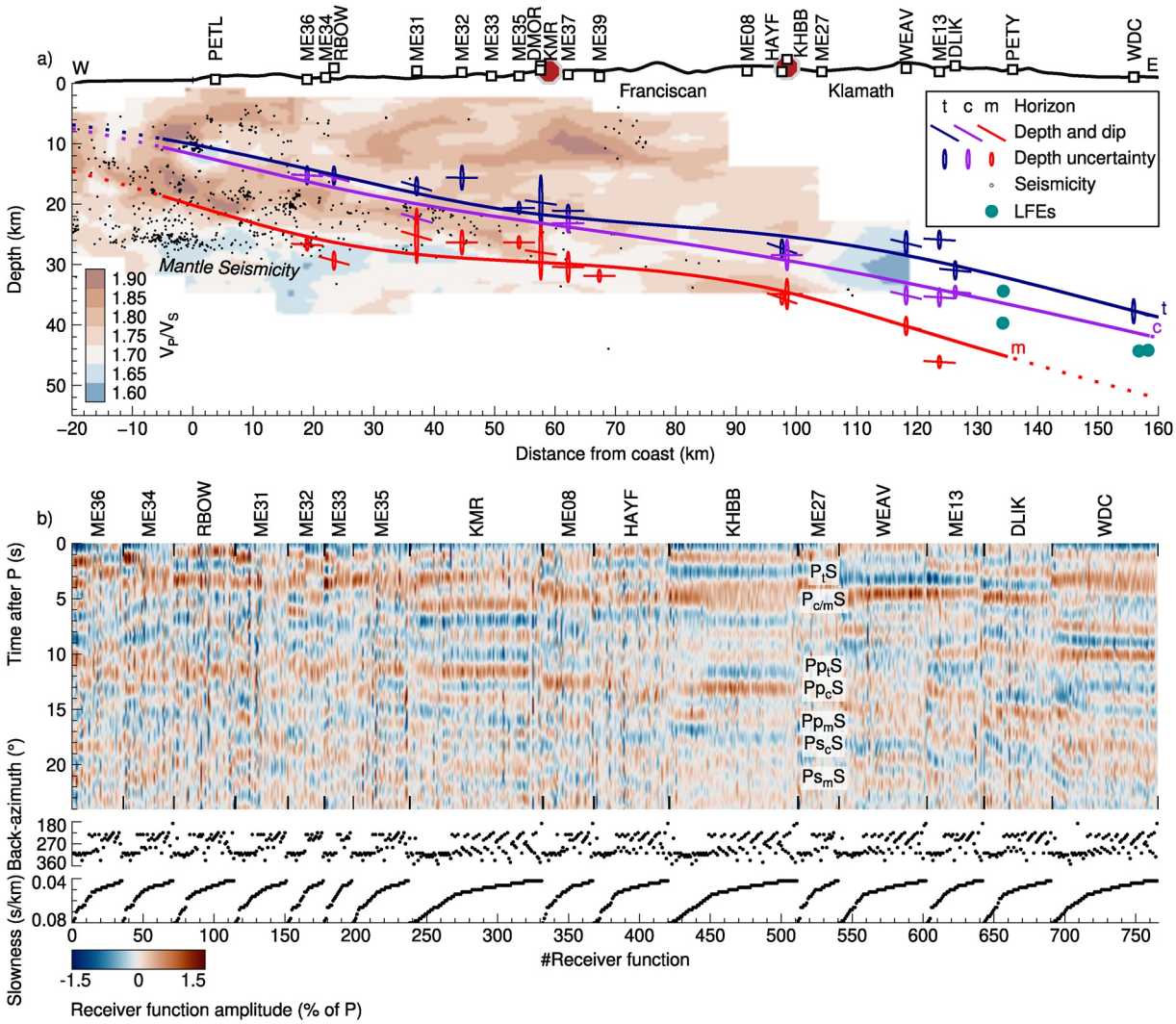

Figure 6. Red octagon marks the intersection of the profile with the terrane backstop.

(*t*, *c*, *m*) brackets weak slab-related seismicity in the offshore area (Morton et al., 2023). It has a thickness of about 7 km near the coast and thickens arc-ward to about 13 km, with the two layers possessing comparable thickness.

3.2.2. Klamath Segment

Beneath the Mendocino region, the subduction stratigraphy has been imaged as a moderately high-V_P/V_S zone (1.8–1.9, Guo et al., 2021) complemented by relatively abundant intraslab seismicity defining a tightly confined Wadati-Benioff zone (e.g., Waldhauser, 2009; Wang & Rogers, 1994; Figure 6). The *t* and *m* horizons encapsulate the seismically active, moderately high-V_P/V_S zone, with the *m* horizon falling in good agreement with the $V_P/V_S = 1.7$ contour. Where it projects beneath the Franciscan terrane, the high-V_P/V_S-zone loses expression and the density of earthquakes diminishes (60 km from coast in Figure 6a). Our slab model here indicates a generally shallower dip that steepens again under the Klamath terrane (100 km from the coast), where it indicates that a low-V_P/V_S anomaly is located within the subduction stratigraphy. Layer 1 is absent between the coast and the Franciscan terrane and attains a thickness of a few kilometers farther landward. Notably, no seismicity is located within Layer 1. The *c* horizon defining the base of Layer 1 approximately aligns with the location of LFEs (Plourde et al., 2015). The entire subduction stratigraphy has a fairly uniform thickness of 10 km. The receiver function slab signature is difficult to correlate laterally, presumably due to some combination of variation in overburden and slab properties (Figure 6b).

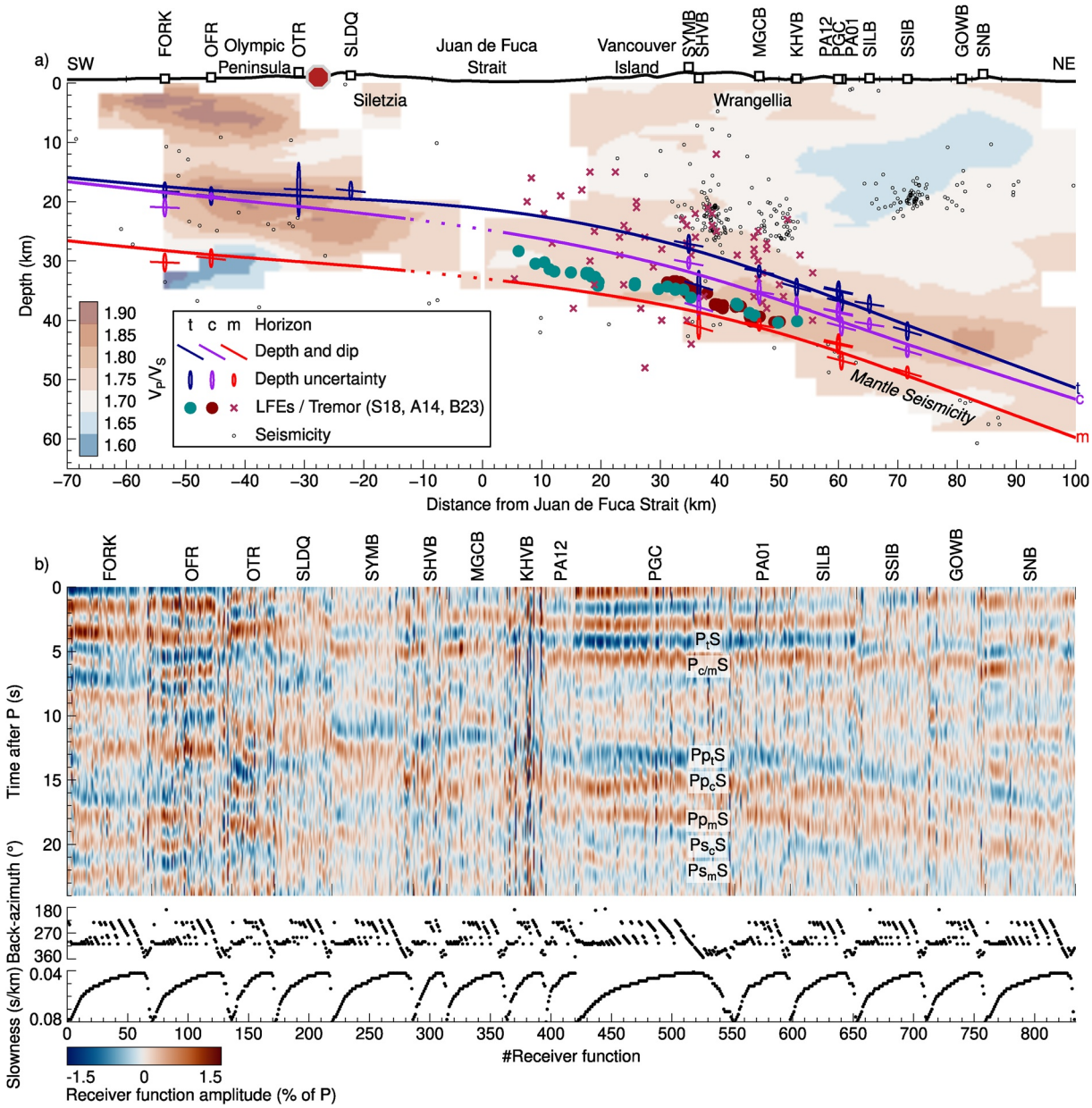

Figure 7. Figure 5 for profile C across the Olympic Peninsula (negative profile distances) and Southern Vancouver Island (positive profile distances). Tomograms and seismicity from Merrill et al. (2020) (Olympic Peninsula) and Savard et al. (2018) (Vancouver Island). Low-frequency earthquake and tremor locations are from: (A14, brown dots) Armbruster et al. (2014); (S18, cyan dots) Savard et al. (2018); and (B23, purple crosses) Bombardier et al. (2023). Comparison with V_S is shown in Figure S55 in Supporting Information S1. Receiver functions were filtered between 2 and 20 s.

3.2.3. Olympic Segment

A profile along the dip from the western end of the Olympic Peninsula, across the Juan de Fuca Strait, southern Vancouver Island, and into the Strait of Georgia reveals a flat lying slab beneath the Olympic Peninsula that continues under the Juan de Fuca Strait and gradually steepens under southern Vancouver Island (Figure 7a). The *t* and *m* horizons encompass the moderately high-V_P/V_S zones previously interpreted as the subducting crust in local seismic tomograms (Merrill et al., 2020; Savard et al., 2018). Under the Olympic Peninsula, this zone is seismically active and *m* agrees well with the $V_P/V_S = 1.7$ contour. Beneath southern Vancouver Island, *m* bounds the top of seismic activity previously interpreted to occur within the subducting mantle (Savard et al., 2018). Layer 1 is absent or very thin beneath the Olympic Peninsula and attains a thickness of about 5 km beneath southern Vancouver Island, where it is aseismic. The *c* horizon is located 2–3 km above

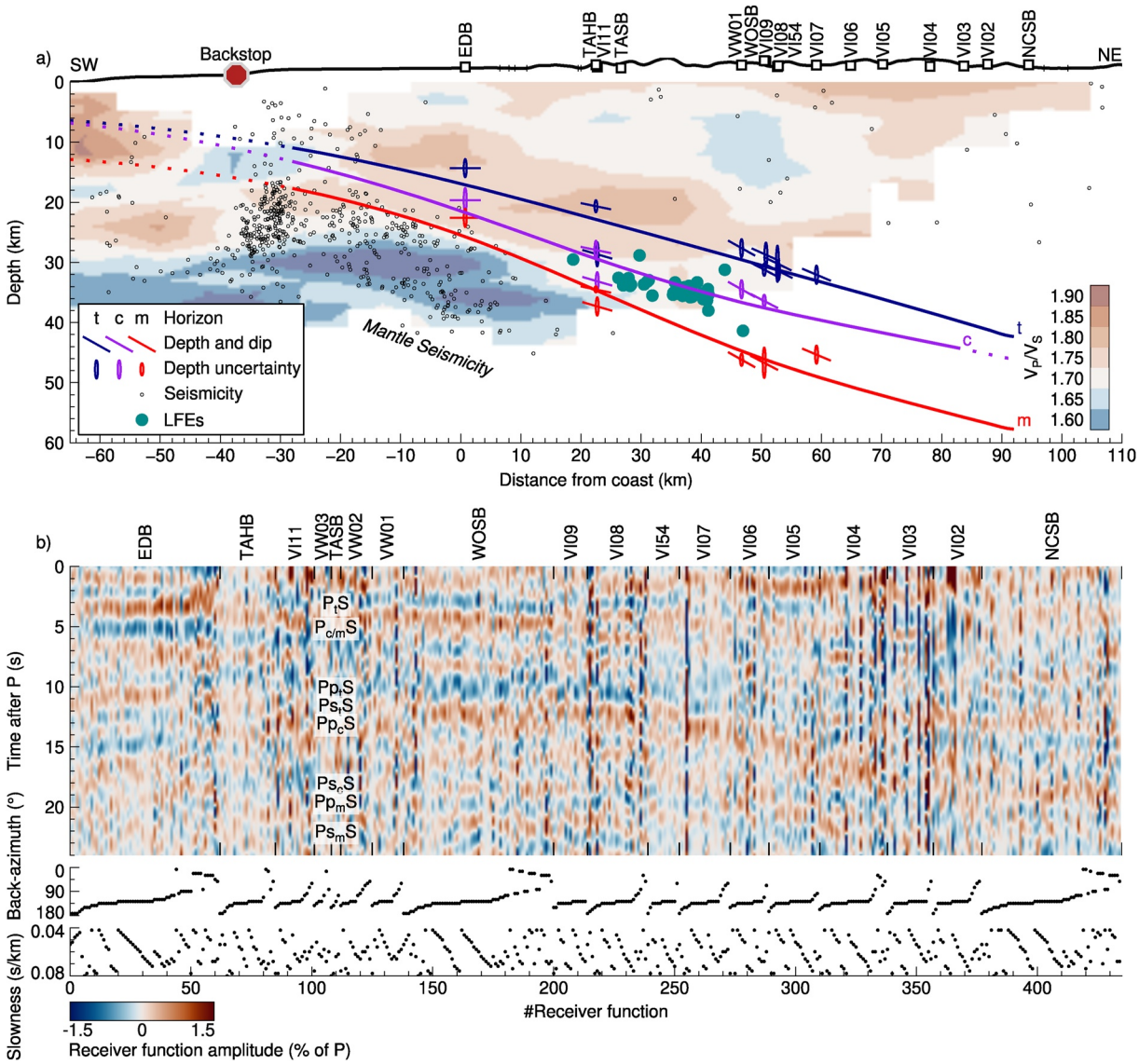

Figure 8. As Figure 5, but for profile D across Northern Vancouver Island. Tomogram and seismicity from Merrill et al. (2022). Low-frequency earthquake locations from Savard et al. (2020). Comparison with V_S is shown in Figure S56 in Supporting Information S1. Receiver functions filtered between 2 and 20 s.

a prominent band of LFE locations (Armbruster et al., 2014; Savard et al., 2018). Tremor hypocenters from Bombardier et al. (2023), see also Kao et al. (2005)) scatter within and above the subduction stratigraphy. The complex overburden structure of the Olympic Peninsula hampers clear identification of *c* and *m*; however, correlations of seismic phases along strike and along dip yield a laterally coherent picture. Beneath southern Vancouver Island, the slab reveals a clear and simple receiver function signature that can be traced beneath the Gulf Islands in the Strait of Georgia and loses expression toward the British Columbia Lower Mainland (Figure 7b).

3.2.4. Vancouver Island Segment

The Vancouver Island segment exhibits *t* and *m* horizons that bracket NE-dipping regions of elevated V_P/V_S evident in local seismic tomograms. The *m* horizon coincides with the $V_P/V_S = 1.7$ contour, that also bounds the top of seismicity which has been inferred to reside in the oceanic mantle (Figure 8a and Figures S3–S16 in Supporting Information S1, Merrill et al., 2022; Savard et al., 2018). *c* can best be seen as a pronounced and distinct horizon in southern and south-central Vancouver Island, where it lies 2–4 km underneath *t* and decisively above LFE locations (Savard et al., 2018).

Toward north-central Vancouver Island, the subduction stratigraphy appears to thicken substantially downdip, from ~8 km near the coast, to ~16 km inland. Layer 1 and Layer 2 contribute in equal part to the combined thickness. The *c* horizon generally follows the LFE locations (Savard et al., 2020). Substantial scatter in the station measurements and difficulties in reconciling phase correlations across closely spaced stations attest to the complex subsurface structures that are also evident in the local seismic tomography and may be related to the subduction of the Nootka Fault Zone as the northern terminus of JdF subduction (Figure 8b, Merrill et al., 2022; Savard et al., 2018).

4. Interpretation of the Subduction Stratigraphy

The combined thickness of the stratigraphic package comprising *t*, *c*, and *m* horizons exceeds almost everywhere the nominal thickness of the incoming oceanic crust of ~6.5 km by 2–12 km (Figure 9a). A thickness of ~7 km is resolved only along the southern Central segment, between ~43° and 44°N. Model regularization may dampen slab complexity and smooth over interface steps on a ~20 km scale (e.g., *m* in Figure 6a), but the excessive thickness of the slab stratigraphy is a robust feature of the model and is almost always underpinned by individual point station measurements. Additional material, other than actively subducting igneous oceanic crust, must therefore make up the subduction stratigraphy.

Layer 2 and the underlying mantle half-space, separated at *m*, were designed to correspond to igneous oceanic crust and pristine mantle. Where seismic velocities and seismicity images are available, the model appears to have captured this contrast appropriately, so that we confidently interpret *m* as the oceanic Moho. We cannot exclude the possibility that, where the plate is hydrated, *m* is biased into the oceanic mantle, lying deeper than the Moho. Signs of mantle hydration may be present under the Cape Mendocino coast and offshore northern Vancouver Island, suggested by a diffuse tomographic Moho, abundant mantle seismicity and the subduction of major fracture zones (Figures 6 and 8, e.g., Chaytor et al., 2004; Merrill et al., 2022; Rohr et al., 2018; Wilson, 1989). Such signatures are, however, not universally present.

The excess thickness is more likely to develop above the plane of active subduction, that is, in Layer 1. Where the thickness of Layer 1 is substantial (i.e., from *t* to *c*; Figure 9b), the E-layer (or a reflective zone above the slab) has been detected in reflection seismic surveys (Figure 9b, Clowes et al., 1987a; Keach et al., 1989; Nedimović et al., 2003; Tréhu et al., 1994). Nedimović et al. (2003) suggest that the emergence of the E-layer is related to the occurrence of ETS. The E-layer is typically thicker than Layer 1, which suggests that Layer 1 is part of the E-layer (Calvert et al., 2020). Within the tremor zone, defined by the 0.1 tremor yr^{-1} km^{-2} contour (Figures 9b–9d; downloaded from https://pnsn.org; Wech, 2010), the mean and median V_P/V_S in Layer 1 are 2.49 ± 0.14 (2σ) and 2.44. Outside the tremor zone V_P/V_S is lower, with a mean value of 2.28 ± 0.14 and median value of 1.95 (Figures 9b, 10a, and 10b). A two-sample Kolmogorov-Smirnov test yields a *p*-value of $5 \cdot 10^{-5}$, indicating that the distribution of V_P/V_S values of Layer 1 from inside and outside the tremor zone are statistically different with >99% confidence. This suggests that the development of Layer 1 as a high-V_P/V_S ULVZ is related to tremor, in agreement with previous findings (Audet et al., 2009; Song et al., 2009). We interpret *t* in the tremor zone as the top of this ULVZ. Projecting the tremor epicenters (Wech, 2010) onto the *t* and *c* horizons yields tremor depths of 32 ± 10.8 and 38 ± 10.2 km (2σ), respectively (Figures 10c and 10d). Tremor depths are concentrated more tightly when projected to the *c* horizon, suggesting that tremor occurs closer to the base of Layer 1 (Figure 9c). Inside the tremor zone, where Layer 1 corresponds to the ULVZ, *c* marks a stark material contrast against the underlying oceanic crust and we interpret *c* as the base of the ULVZ.

Between the coast and the tremor zone, except between 44° and 45°N, Layer 1 is typically thinner (Figure 9b) and its V_P/V_S is lower (Figures 9d and 10b), attaining normal values for basaltic material (~1.8). Layers 1 and 2 still exhibit a combined thickness in excess of the incoming oceanic crust, with Layer 1 displaying properties that are nevertheless similar to oceanic crust. The *t* horizon is here the top of this excess volume. The *c* horizon here usually marks a less prominent material contrast than inside the tremor zone. It may seem natural to interpret *c* as the base of a possible sedimentary blanket above an underlying igneous oceanic crust (e.g., Delph et al., 2018), but we note here that Layer 2 is frequently thicker than oceanic crust, hence the interpretation of *c* as the base of sediments is possible but not universal. Horizon *c* may alternatively represent a velocity gradient within a sedimentary layer or the base of altered material belonging to the overriding continental crust.

10.1029/2023GC011088

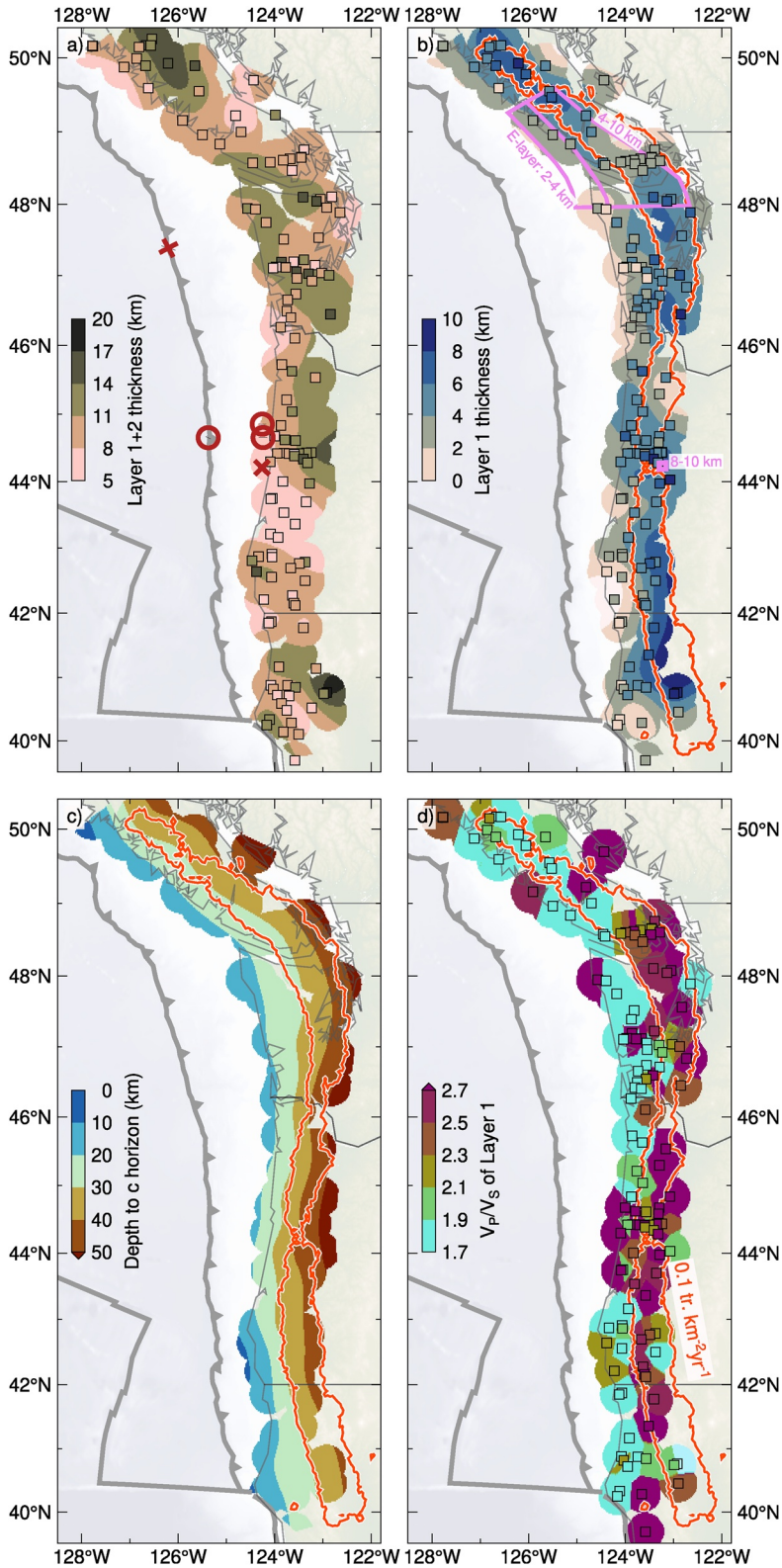

Figure 9. Select properties of slab stratigraphy. (a) Combined Layers 1 and 2 (*t*-to-*m*) thickness. "O" mark places where sediment subduction has been detected on marine seismic surveys, "X" where sediment subduction is absent (Han et al., 2016; Tréhu et al., 2012). The thickness of the subduction stratigraphy exceeds the thickness of the igneous oceanic crust. (b) Layer 1 (*t*-to-*c*) thickness and tremor zone (Wech, 2010). Downdip thickening of Layer 1 correlates with tremor locations. (c) Depth to *c* horizon correlates closely with tremor occurrence (Figures 10c and 10d). (d) V_P/V_S of Layer 1.

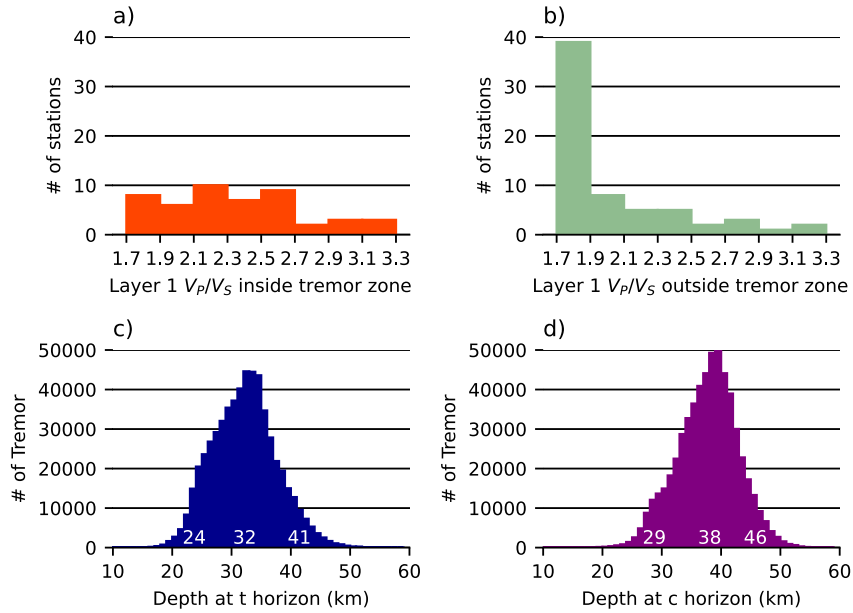

Figure 10. Properties of Layer 1 in relation to tremor (a, b) V_P/V_S of Layer 1 at stations (a) inside and (b) outside the tremor zone (0.1 tremor km^{-2} yr^{-1} contour; Figure 9) (c, d). Depth distribution of tremor epicenters projected onto the (c) *t* and (d) *c* horizons. Numbers at the base indicate the 5%, 50%, and 95% quantiles of the depth distribution.

5. Discussion

5.1. Possible Controls on Slab Morphology

The overall slab morphology exhibits a first-order correlation with the location of the static backstops in the Cascadia subduction system (Figure 11, Watt & Brothers, 2020). These are kinematic discontinuities that are related to distinct strength contrasts within the continental crust formed by accreted crystalline terranes. The most important terrane is Siletzia, a basaltic large igneous province that formed offshore as an oceanic plateau, possibly related to magmatism of the Yellowstone hotspot. It can be mapped along coastal Oregon, Washington and British Columbia (Wells et al., 2014). An associated aeromagnetic anomaly indicates that Siletzia is most voluminous in central and northern Oregon (Wells et al., 1998). Reflection seismic together with wide-angle seismic data and geomorphologic markers reveal that the base of Siletzia is up to 35 km deep and possibly extends down to the plate interface (Tréhu et al., 1994). This inference is substantiated by magneto-telluric data that image a voluminous resistive body, interpreted as representing Siletzia, that meets the plate interface in coastal Oregon (Egbert et al., 2022). Kinematically, the thickened Siletz terrane forms a distinct block that rotates clockwise with respect to stable North America (Wells et al., 1998) and displays the lowest interseismic vertical uplift rates along the entire forearc (Mitchell et al., 1994). Where the Siletz terrane recedes far inland on the eastern side of the Olympic Peninsula, giving way to the Olympic complex formed by underthrust marine sediments (e.g., Brandon & Calderwood, 1990), the slab lies shallower and flatter than anywhere else along the entire onshore forearc. Conversely, where the western boundary of the Siletz terrane is located off-shore and Siletzia is thickest, the slab is deepest and has its steepest dip (Figure 11). This suggests that the competence and rigidity of the Siletz block force the descent of the Juan de Fuca slab. It has been suggested that the Kumano pluton influences the subducting Philippine Sea Plate in a similar manner below southwest Japan (Arnulf et al., 2022).

In between the shallowly dipping Olympic and steeply dipping Central segments, a pronounced southward downward bend in the slab is evident along a line extending between Grays Harbor and the southern end of Puget Sound. The bend can be seen in the raw receiver functions, where the timing of the P_mS conversion increases, for example, from ~3 to ~4 s for rays arriving from NNW relative to those arriving from SSE azimuths at station US.NLWA and again from 4 to 4.5 s just south of that at station UW.WISH (Figure 12). Perhaps significantly, the three largest intermediate depth earthquakes in Cascadia, the 1949 *M*6.7 Olympia (Nuttli, 1952), 1965 *M*6.7 Puget Sound (Langston & Blum, 1977), and 2001 *M*6.8 (Ichinose et al., 2004; Kao et al., 2008) earthquakes occurred near the down-dip continuation of this bend, at depths at or immediately below those projected for the oceanic Moho.

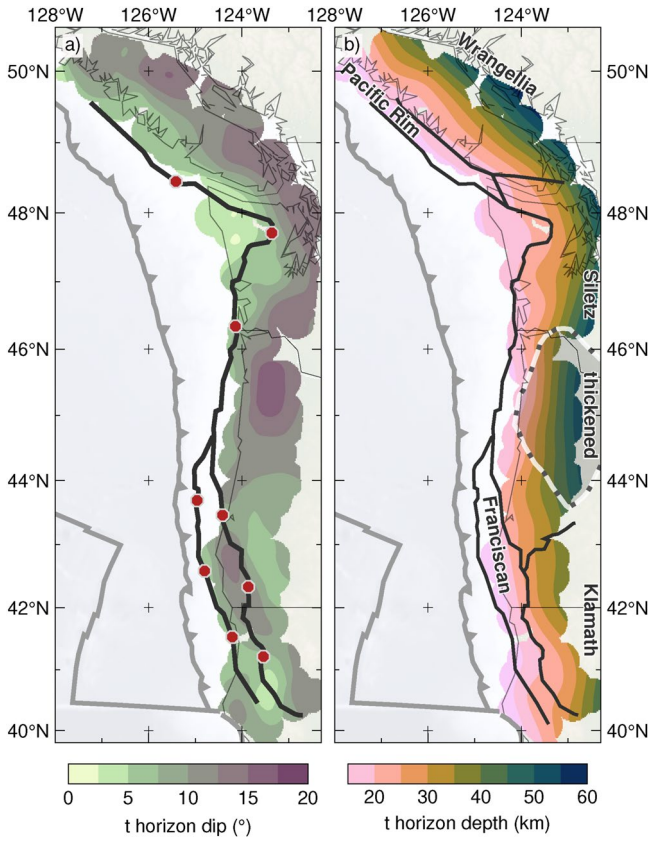

Figure 11. (a) Dip and (b) depth of the *t* horizon. Static backstop (line with red octagons in panel (a)) and terrane boundaries (thick lines in panel (b)) modified after Watt and Brothers (2020). Shaded area enclosed by white dashed line represents thickened Siletz terrane detected in aeromagnetic data (after Wells et al. (1998)). The location of the terrane backstop correlates with and may exert a first order control on slab morphology.

Along the Klamath segment to the south (south of 44°N), the slab structure is complex. The Gorda Plate, a relatively young and highly deformed plate (Chaytor et al., 2004; Wilson, 1989), encounters two static backstops, namely the western boundaries of the Franciscan complex and the Klamath terrane (Figure 11, Clarke, 1992; Watt & Brothers, 2020), and is bounded to the south by the Mendocino Fracture Zone. The southern and eastward trending seaward boundary of the thickened Siletz terrane has a reduced impact on slab morphology, resulting in the southward transition to a more gently dipping slab (Figure 11). This geometry is interrupted with the emergence of the Klamath terrane, where the steepest dip of the slab is located near the coast, bending behind the first (seaward) backstop, and unbending beneath the second (landward) backstop. In the Cape Mendocino area, the slab top is contorted in a fashion that yields a flat-lying segment just behind the coast. Because of the generally lower dip in advance of the volcanic arc and its unbending beneath the southern Siletz and Klamath terranes, it appears as if the Gorda plate does not subduct as readily as the Juan de Fuca plate. A possible cause for this behavior is increased buoyancy of the youngest subducting lithosphere (5–6 Ma at the trench, e.g., Wilson, 1993).

5.2. Excess Thickness of Subduction Stratigraphy

The nature and origin of the E-layer as a prominent element of the subduction zone stratigraphy that emerges abruptly along the dip trajectory in the vicinity of southern Vancouver Island is a long-standing conundrum in the understanding of the Cascadia subduction zone (e.g., Calvert, 1996; Calvert et al., 2011, 2020; Clowes et al., 1987a; Nedimović et al., 2003). Our data show a qualitative correlation between a thick Layer 1 and a thick (>4 km) E-layer where the latter has been imaged (Figure 9b). We also suggest that the reflective zone mapped by COCORP in central Oregon (Figure 9b, Keach et al., 1989) may manifest the presence of a structure with similar origin since it also coincides with a thick Layer 1. Assuming this association holds true along the entire margin, our data suggest that the E-layer is ubiquitous. Its abrupt emergence along dip is likewise reflected in our data: Coastal stations have a tendency to exhibit a thin or absent Layer 1, whereas inland stations generally possess a thick one (Figure 9b), consistent with previous inferences of Layer 1 thickening near the coast line from an amphibious receiver function study (Audet & Schaeffer, 2018). Interestingly, the combined (Layer 1 + Layer 2) thickness of the subduction stratigraphy does not obey the same trend. Places of a thin or absent Layer 1 may have an overall thick subduction stratigraphy (e.g., coastal Olympic Peninsula and Cape Mendocino) and a significantly thick Layer 1 may correspond to a subduction stratigraphy that does not much exceed the thickness of the incoming oceanic crust (e.g., ~7 km thickness between 43° and 44°N; Figure 13a).

Sediments entering the subduction system may contribute to the subduction stratigraphy (e.g., Delph et al., 2018), but information about the amount of subducting sediment at the time of writing is scarce. Tréhu et al. (2012) interpret sediments subducting beneath Siletzia on two seismic lines near 45°N (circles on Figure 9a), but not on a third line closer to 44°N (cross on Figure 9a). Within the same latitude interval, the characteristic transition from thickened to normal subduction stratigraphy occurs, suggesting that these subducting sediments make up for the extra thickness (Figure 13b). In contrast, Han et al. (2016) document no sediment subduction at the latitude of the Juan de Fuca Strait, where we image thick (~11 km) subduction stratigraphy. However, it is possible that sediment subduction occurred at the trench in the latter region at 3 Ma ago, and subsequently ceased. More data are required to conclusively define where sediment subduction contributes to subduction stratigraphy thickness.

We note that Layer 1 emerges at around 30 km depth and gains thickness along the subduction trajectory, and that this thickness is unrelated to the thickness of the subduction stratigraphy updip of this depth (Figures 9a and 9b). This observation suggests that Layer 1 thickens in situ and develops a ULVZ through some depth-activated process. Elevated $V_P/V_S > 2.0$ (Figures 9b and 9d) suggest that the medium is fractured and saturated with

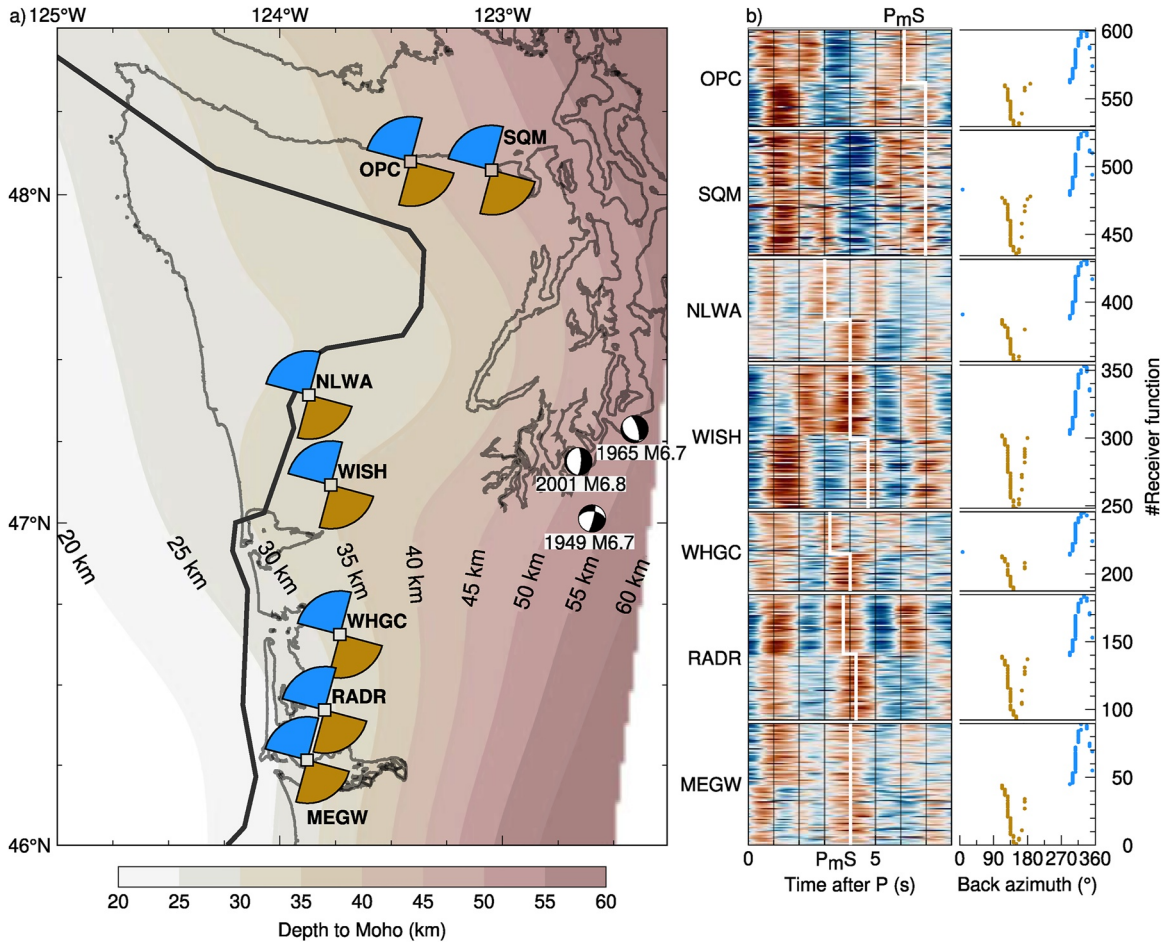

Figure 12. Downwarped Moho from the Olympic Peninsula to Grays Harbor. (a) Map view with Moho depth contours as well as locations and receiver function ray back azimuths of stations shown on the right. Earthquake locations and focal mechanisms from International Seismological Centre (2023). (b) Radial receiver functions sorted by back azimuth. Rays arriving from NNW colored blue and from SSW colored gold. Note the southward down Moho-steps (P_mS) at stations coincident with a thickening low velocity zone above at stations NLWA, WISH, WHGC, and RADR.

pressurized fluids (Christensen, 1984), implying that it has lost structural integrity and strength. As a weak zone, the ULVZ is likely to host slip (e.g., Luo & Liu, 2021; Wech & Creager, 2011). LFE hypocenters are located near the base of the ULVZ (Figure 14, Calvert et al., 2020), suggesting that the plate boundary is located near *c*. Excess thickness may be due to underplating of subducting material, either of sediments atop the oceanic crust (e.g., Delph et al., 2018) or of the upper basaltic crust, which may lose structural integrity through wear (Figure 13c, see also e.g., Calvert et al., 2020; Clowes et al., 1987a). Moderately high seismic velocities ($V_S > 3.2$ and $V_P/V_S < 1.9$) indicated by our inverse modeling results for Layer 2 (Figure 2 and Figure S51 in Supporting Information S1) preclude the presence of pervasive fracturing and pressurized fluids (Christensen, 1984). Instead, the presence of slivers of oceanic crust, large enough to *not* reduce seismic velocities significantly, would be consistent with LFE occurrence inside Layer 2. The subordinate slip represented by the LFEs during ETS episodes is consistent with the process of initiating detachment of the subducting oceanic crust at the LFE horizon (Figure 13c). Slow slip, which makes up the main share of the slip budget at depth (Bostock et al., 2015; Dragert et al., 2001, 2004; Kao et al., 2010), may well be located at or above *c*, that is, at the base or inside the 4–10 km thick ULVZ.

Subcretion and underplating are consistent with earlier inferences made for the onshore Cascadia forearc from a wealth of geophysical data. Calvert et al. (2011) interpret underplating of sediments as taking place south of Puget Sound. Calvert (2004) and Clowes et al. (1987a) inferred that the E-layer constitutes underplated metabasaltic material beneath southern Vancouver Island based on high seismic velocities. The correspondence between these

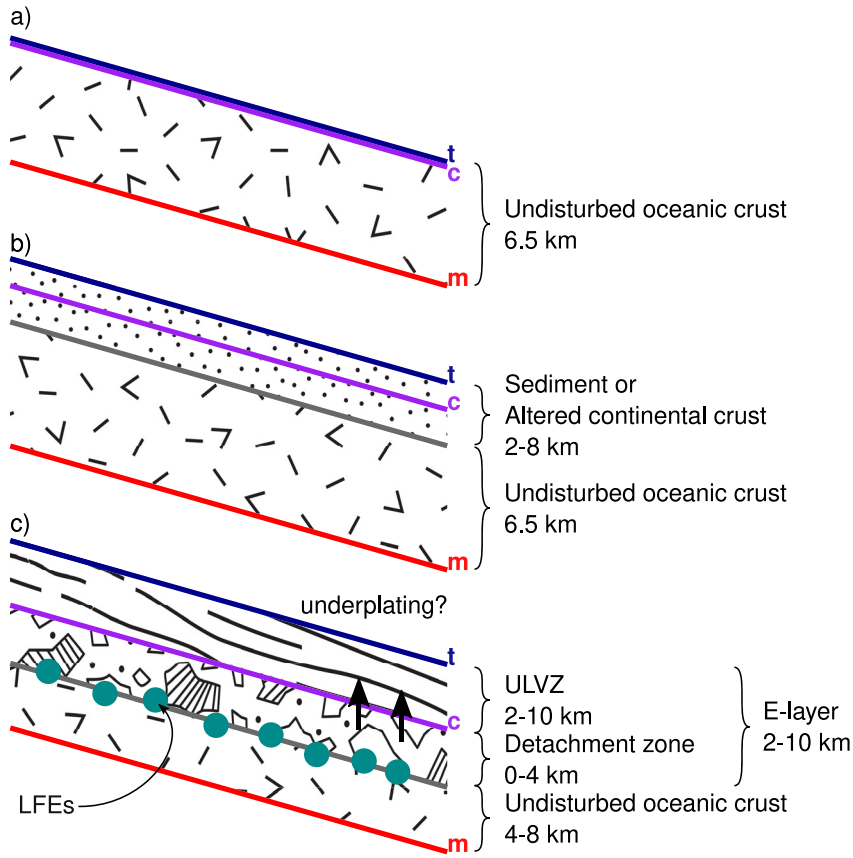

Figure 13. Possible subduction stratigraphies present in the Cascadia subduction zone. (a) Subduction of undisturbed oceanic crust (e.g., Central–South Oregon). (b) Sediment subduction, *c* may represent the base of the sedimentary later or a horizon within the sediments (e.g., Olympic Peninsula, Northern Oregon). (c) E-layer on top of the subducting crust. Low-frequency earthquake locations may indicate a detachment horizon at or below the base of the ultralow *S*-wave velocity zone. Low seismic velocities and in situ thickening above suggest ongoing underplating (e.g., Southern Vancouver Island).

inferred sites of underplating with the thick ULVZ detected here and the widespread distribution of the ULVZ suggest that underplating is occurring through the majority of the entire Cascadia forearc (e.g., Delph et al., 2021).

6. Conclusion

Receiver functions provide valuable insights into the subduction of the Juan de Fuca and Gorda plates in the Cascadia region. Based on previous studies of receiver-side forward and back-scattered mode conversions, we parameterize subduction stratigraphy in three horizons *t*, *c*, and *m*. Mapping these horizons across the forearc reveals flatter slab segments beneath the Olympic Peninsula and Cape Mendocino, central Oregon exhibits a steeply dipping slab. Below most of Vancouver Island, the slab is marked by modest dips (~7°–12°). This slab morphology appears to be influenced by the mechanical strength and density of accreted crystalline terranes. A notable Moho step south of the Olympic Peninsula may relate to recurrent, large, intermediate-depth earthquakes beneath Puget Sound. In addition, the presence of a thick topmost layer in the subduction stratigraphy may indicate the widespread occurrence of the E-layer. Previous interpretations suggest that the E-layer represents underplated slab material, including both sediments and metabasalt, implying that underplating occurs through most of the Cascadia forearc.

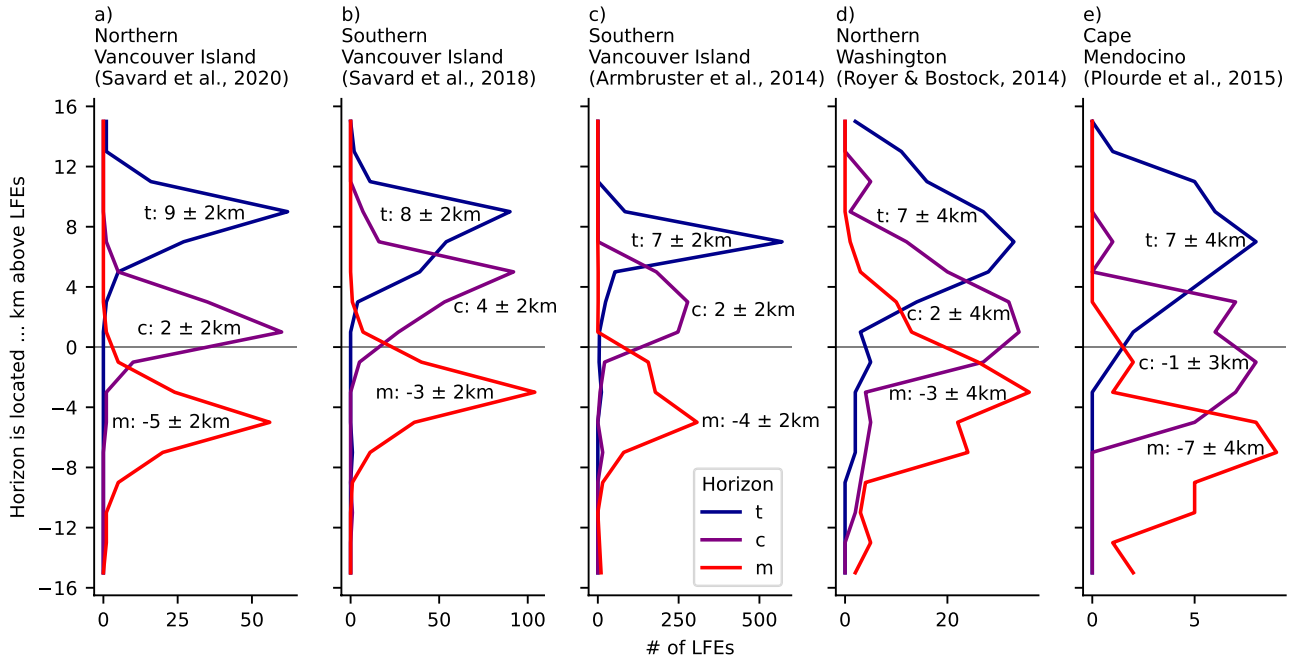

Figure 14. Histograms of the depth of *t*, *c*, and *m* horizons relative to low-frequency earthquake (LFE) locations for different regions. Bin width is 2 km. LFEs are most closely located to the *c* horizon. For Vancouver Island, the data indicate that LFEs occur in Layer 2 between *c* and *m*.

Data Availability Statement

The model parameters and slab horizons are part of the Data Set S1 of this manuscript and with the additional raw receiver functions, available through GFZ Data Services (Bloch et al., 2023). The networks with the following FDSN network coded were used in this study: BK (Northern California Earthquake Data Center, 2014), C8, CC (Cascades Volcano Observatory & USGS, 2001), CN (Natural Resources Canada (NRCAN Canada), 1975), IU (Albuquerque Seismological Laboratory & USGS, 2014), NC (USGS Menlo Park, 1966), PO, TA (IRIS Transportable Array, 2003), UO (University of Oregon, 1990), US (Albuquerque Seismological Laboratory (ASL) & USGS, 1990), UW (University of Washington, 1963), X4 (2016–2021, Cakir, 2016), XA (2008–2009, Trehu & Williams, 2008), XD (2014–2016, Creager, 2014), XQ (2007–2009, Levander, 2007), XU (2006–2012, Malone et al., 2006), XZ (1993–1994), YS (2001–2003, Brodsky, 2001), and YW (2007–2010, Brudzinski & Allen, 2007). Seismic waveforms are available via the IRIS Data Management Center (IRISDMC, http://service.iris.edu/fdsnws/dataselect/1/), the Northern California Earthquake Data Center (https://service.ncedc.org/fdsnws/dataselect/1/), and the Natural Resources Canada Data Center (https://earthquakescanada.nrcan.gc.ca/fdsnws/dataselect/1/).

Acknowledgments
We thank Suzanne Carbotte for the generous and substantive discussion and preview of CASIE'21 results. Hao Guo, Jeffrey McGuire, Leo Kan, Sebastien Chevrot, Reid Merrill, and Genevieve Savard kindly made their seismic tomograms and relocated seismicity available. Paul Wessel and the *GMT* community supported the computation of regularized spline surfaces. Discussions with Raul Mendoza and Simon Peacock provided valuable insights into Cascadia forearc architecture. Madison Bombardier tested the Data Set S1. Leonardo Colavitti and an anonymous reviewer provided valuable comments that helped to improve the manuscript. This research was funded

References

Abers, G. A., MacKenzie, L. S., Rondenay, S., Zhang, Z., Wech, A. G., & Creager, K. C. (2009). Imaging the source region of Cascadia tremor and intermediate-depth earthquakes. *Geology*, *37*(12), 1119–1122. https://doi.org/10.1130/g30143a.1

Albuquerque Seismological Laboratory, (ASL), & USGS. (1990). United States national seismic network [Dataset]. International Federation of Digital Seismograph Networks. https://doi.org/10.7914/SN/US

Albuquerque Seismological Laboratory, (ASL), & USGS. (2014). Global seismograph network (GSN - IRIS/USGS) [Dataset]. International Federation of Digital Seismograph Networks. https://doi.org/10.7914/SN/IU

Armbruster, J. G., Kim, W.-Y., & Rubin, A. M. (2014). Accurate tremor locations from coherent S and P waves. *Journal of Geophysical Research: Solid Earth*, *119*(6), 5000–5013. https://doi.org/10.1002/2014jb011133

Arnulf, A. F., Bassett, D., Harding, A. J., Kodaira, S., Nakanishi, A., & Moore, G. (2022). Upper-plate controls on subduction zone geometry, hydration and earthquake behaviour. *Nature Geoscience*, *15*(2), 143–148. https://doi.org/10.1038/s41561-021-00879-x

Aster, R. C., Borchers, B., & Thurber, C. H. (2018). *Parameter estimation and inverse problems*. Elsevier.

Audet, P. (2020). RfPy: Teleseismic receiver function calculation and post-processing [Dataset]. Zenodo. https://doi.org/10.5281/ZENODO.4302558

Audet, P., & Bloch, W. (2022). PyRaysum: Software for modeling ray-theoretical body-wave propagation [Software]. Zenodo. https://doi.org/10.5281/ZENODO.7468301

Audet, P., Bostock, M. G., Boyarko, D. C., Brudzinski, M. R., & Allen, R. M. (2010). Slab morphology in the Cascadia fore arc and its relation to episodic tremor and slip. *Journal of Geophysical Research*, *115*, B00A16. https://doi.org/10.1029/2008jb006053

by Deutsche Forschungsgemeinschaft Grant BL 1758/1-1 to WB, and NSERC Discovery Grants RGPIN-2021-03039 to MGB and RGPIN-2018-03752 to PA. This research regards the ancestral homelands and waters of hundreds of diverse and distinct Indigenous Peoples. Among them are the Kwakwaka'wakw Peoples, the Nuu-chah-nulth Peoples, the Makah Peoples, the Coast Salish Peoples, the Quileute Peoples, the Chinookan Peoples, the Siletz People, the Cow Creek Band, the Grand Ronde Community, the Coos, Lower Umpqua, and Siuslaw Peoples, the Klamath Tribes, the Hupa People, the Yurok People, and the Karuk People. It was undertaken at the UBC Vancouver campus on the traditional, ancestral, and unceded territories of the Musqueam People and at the University of Ottawa, located on unceded Algonquin territory. Kayla Lar-Son of UBC's Xwi7xwa Library provided assistance in the formulation of this land acknowledgment.

Audet, P., Bostock, M. G., Christensen, N. I., & Peacock, S. M. (2009). Seismic evidence for overpressured subducted oceanic crust and megathrust fault sealing. *Nature*, *457*(7225), 76–78. https://doi.org/10.1038/nature07650

Audet, P., Bostock, M. G., Mercier, J.-P., & Cassidy, J. F. (2008). Morphology of the Explorer–Juan de Fuca slab edge in northern Cascadia: Imaging plate capture at a ridge-trench-transform triple junction. *Geology*, *36*(11), 895–898. https://doi.org/10.1130/G25356A.1

Audet, P., & Schaeffer, A. J. (2018). Fluid pressure and shear zone development over the locked to slow slip region in Cascadia. *Science Advances*, *4*(3), eaar2982. https://doi.org/10.1126/sciadv.aar2982

Bar, N., Long, M. D., Wagner, L. S., Beck, S. L., Zandt, G., & Tavera, H. (2019). Receiver function analysis reveals layered anisotropy in the crust and upper mantle beneath southern Peru and northern Bolivia. *Tectonophysics*, *753*, 93–110. https://doi.org/10.1016/j.tecto.2019.01.007

Bloch, W., & Audet, P. (2023). PyRaysum: Software for modeling ray-theoretical plane body-wave propagation in dipping anisotropic media. *Seismica*, *2*(1). https://doi.org/10.26443/seismica.v2i1.220

Bloch, W., Bostock, M. G., & Audet, P. (2023). Forearc on-shore receiver functions, station subsurface models, and fitted slab model for Cascadia [Dataset]. GFZ Data Services. https://doi.org/10.5880/fidgeo.2023.033

Bloch, W., John, T., Kummerow, J., Salazar, P., Krüger, O. S., & Shapiro, S. A. (2018). Watching dehydration: Seismic indication for transient fluid pathways in the oceanic mantle of the subducting Nazca slab. *Geochemistry, Geophysics, Geosystems*, *19*(9), 3189–3207. https://doi.org/10.1029/2018gc007703

Bombardier, M., Dosso, S. E., Cassidy, J. F., & Kao, H. (2023). Tackling the challenges of tectonic tremor localization using differential travel-times and Bayesian inversion. *Geophysical Journal International*, *234*(1), 479–493. https://doi.org/10.1093/gji/ggad086

Bostock, M. G. (1998). Mantle stratigraphy and evolution of the slave province. *Journal of Geophysical Research*, *103*(B9), 21183–21200. https://doi.org/10.1029/98jb01069

Bostock, M. G., Hyndman, R. D., Rondenay, S., & Peacock, S. (2002). An inverted continental Moho and serpentinization of the forearc mantle. *Nature*, *417*(6888), 536–538. https://doi.org/10.1038/417536a

Bostock, M. G., Thomas, A. M., Savard, G., Chuang, L., & Rubin, A. M. (2015). Magnitudes and moment-duration scaling of low-frequency earthquakes beneath southern Vancouver Island. *Journal of Geophysical Research: Solid Earth*, *120*(9), 6329–6350. https://doi.org/10.1002/2015jb012195

Brandon, M. T., & Calderwood, A. R. (1990). High-pressure metamorphism and uplift of the Olympic subduction complex. *Geology*, *18*(12), 1252. https://doi.org/10.1130/0091-7613(1990)018⟨1252:hpmauo⟩2.3.co;2

Brodsky, E. (2001). Observational constraints on persistent water level changes generated by seismic waves [Dataset]. International Federation of Digital Seismograph Networks. https://doi.org/10.7914/SN/YS_2001

Brudzinski, M., & Allen, R. (2007). Resolving structural control of episodic tremor and slip along the length of Cascadia [Dataset]. International Federation of Digital Seismograph Networks. https://doi.org/10.7914/SN/YW_2007

Cakir, R. (2016). Monitoring active faults for tectonic mapping efforts in Washington state [Dataset]. International Federation of Digital Seismograph Networks. https://doi.org/10.7914/SN/X4_2016

Caldwell, W. B., Klemperer, S. L., Lawrence, J. F., Rai, S. S., & Ashish (2013). Characterizing the main Himalayan thrust in the Garhwal Himalaya, India with receiver function CCP stacking. *Earth and Planetary Science Letters*, *367*, 15–27. https://doi.org/10.1016/j.epsl.2013.02.009

Calvert, A. J. (1996). Seismic reflection constraints on imbrication and underplating of the northern Cascadia convergent margin. *Canadian Journal of Earth Sciences*, *33*(9), 1294–1307. https://doi.org/10.1139/e96-098

Calvert, A. J. (2004). Seismic reflection imaging of two megathrust shear zones in the northern Cascadia subduction zone. *Nature*, *428*(6979), 163–167. https://doi.org/10.1038/nature02372

Calvert, A. J., Bostock, M. G., Savard, G., & Unsworth, M. J. (2020). Cascadia low frequency earthquakes at the base of an overpressured subduction shear zone. *Nature Communications*, *11*(1), 3874. https://doi.org/10.1038/s41467-020-17609-3

Calvert, A. J., & Clowes, R. M. (1991). Seismic evidence for the migration of fluids within the accretionary complex of western Canada. *Canadian Journal of Earth Sciences*, *28*(4), 542–556. https://doi.org/10.1139/e91-048

Calvert, A. J., Preston, L. A., & Farahbod, A. M. (2011). Sedimentary underplating at the Cascadia mantle-wedge corner revealed by seismic imaging. *Nature Geoscience*, *4*(8), 545–548. https://doi.org/10.1038/ngeo1195

Calvert, A. J., Ramachandran, K., Kao, H., & Fisher, M. A. (2006). Local thickening of the Cascadia forearc crust and the origin of seismic reflectors in the uppermost mantle. *Tectonophysics*, *420*(1–2), 175–188. https://doi.org/10.1016/j.tecto.2006.01.021

Carbotte, S. M., Boston, B., Han, S., Shuck, B., Canales, J. P., Beeson, J. W., et al. (2022). New observations of plate interface depth and geometry at the offshore Cascadia subduction zone from the CAscadia Seismic Imaging Experiment 2021 (CASIE21) and comparisons with existing plate depth models. In *AGU Fall Meeting abstracts* (Vol. 2022, p. S46B-01).

Carbotte, S. M., Han, S., Boston, B., & Canales, J. (2023). Processed pre-stack depth-migrated seismic reflection data from the 2021 CASIE21 multi-channel seismic survey (MGL2104) [Dataset]. Interdisciplinary Earth Data Alliance (IEDA). https://doi.org/10.26022/IEDA/331274

Cascades Volcano Observatory, & USGS. (2001). Cascade chain volcano monitoring [Dataset]. International Federation of Digital Seismograph Networks. https://doi.org/10.7914/SN/CC

Cassidy, J. F., & Ellis, R. M. (1993). S wave velocity structure of the northern Cascadia subduction zone. *Journal of Geophysical Research*, *98*(B3), 4407–4421. https://doi.org/10.1029/92JB02696

Chaytor, J. D., Goldfinger, C., Dziak, R. P., & Fox, C. G. (2004). Active deformation of the Gorda plate: Constraining deformation models with new geophysical data. *Geology*, *32*(4), 353–356. https://doi.org/10.1130/g20178.2

Chen, L., Wen, L., & Zheng, T. (2005). A wave equation migration method for receiver function imaging: 2. Application to the Japan subduction zone. *Journal of Geophysical Research*, *110*(B11), B11310. https://doi.org/10.1029/2005jb003666

Christensen, N. I. (1984). Pore pressure and oceanic crustal seismic structure. *Geophysical Journal International*, *79*(2), 411–423. https://doi.org/10.1111/j.1365-246x.1984.tb02232.x

Christensen, N. I. (1996). Poisson's ratio and crustal seismology. *Journal of Geophysical Research*, *101*(B2), 3139–3156. https://doi.org/10.1029/95jb03446

Clarke, S. H. (1992). Geology of the Eel River basin and adjacent region: Implications for late cenozoic tectonics of the southern Cascadia subduction zone and Mendocino triple junction (1). *AAPG Bulletin*, *76*, 199–224. https://doi.org/10.1306/bdff87ae-1718-11d7-8645000102c1865d

Clowes, R. M., Brandon, M. T., Green, A. G., Yorath, C. J., Brown, A. S., Kanasewich, E. R., & Spencer, C. (1987a). LITHOPROBE—Southern Vancouver island: Cenozoic subduction complex imaged by deep seismic reflections. *Canadian Journal of Earth Sciences*, *24*(1), 31–51. https://doi.org/10.1139/e87-004

Clowes, R. M., Yorath, C., & Hyndman, R. (1987b). Reflection mapping across the convergent margin of western Canada. *Geophysical Journal International*, *89*(1), 79–84. https://doi.org/10.1111/j.1365-246x.1987.tb04391.x

Colavitti, L., Hetényi, G., & the AplArray Working Group. (2022). A new approach to construct 3-D crustal shear-wave velocity models: Method description and application to the Central Alps. *Acta Geodaetica et Geophysica*, *57*(4), 529–562. https://doi.org/10.1007/s40328-022-00394-4

Crameri, F., Shephard, G. E., & Heron, P. J. (2020). The misuse of colour in science communication. *Nature Communications*, *11*(1), 1–10. https://doi.org/10.1038/s41467-020-19160-7

Creager, K. (2014). Collaborative research: Illuminating the architecture of the greater Mount St. Helens magmatic systems from slab to surface [Dataset]. International Federation of Digital Seismograph Networks. https://doi.org/10.7914/SN/XD_2014

Delph, J. R., Levander, A., & Niu, F. (2018). Fluid controls on the heterogeneous seismic characteristics of the Cascadia margin. *Geophysical Research Letters*, *45*(20), 11021–11029. https://doi.org/10.1029/2018GL079518

Delph, J. R., Thomas, A. M., & Levander, A. (2021). Subcretionary tectonics: Linking variability in the expression of subduction along the Cascadia forearc. *Earth and Planetary Science Letters*, *556*, 116724. https://doi.org/10.1016/j.epsl.2020.116724

DeMets, C., Gordon, R. G., Argus, D. F., & Stein, S. (1994). Effect of recent revisions to the geomagnetic reversal time scale on estimates of current plate motions. *Geophysical Research Letters*, *21*(20), 2191–2194. https://doi.org/10.1029/94gl02118

Dragert, H., Wang, K., & James, T. S. (2001). A silent slip event on the deeper Cascadia subduction interface. *Science*, *292*(5521), 1525–1528. https://doi.org/10.1126/science.1060152

Dragert, H., Wang, K., & Rogers, G. (2004). Geodetic and seismic signatures of episodic tremor and slip in the northern Cascadia subduction zone. *Earth Planets and Space*, *56*(12), 1143–1150. https://doi.org/10.1186/bf03353333

Egbert, G. D., Yang, B., Bedrosian, P. A., Key, K., Livelybrooks, D. W., Schultz, A., et al. (2022). Fluid transport and storage in the Cascadia forearc influenced by overriding plate lithology. *Nature Geoscience*, *15*(8), 677–682. https://doi.org/10.1038/s41561-022-00981-8

Flück, P., Hyndman, R. D., & Wang, K. (1997). Three-dimensional dislocation model for great earthquakes of the Cascadia subduction zone. *Journal of Geophysical Research*, *102*(B9), 20539–20550. https://doi.org/10.1029/97jb01642

Flueh, E. R., Fisher, M. A., Bialas, J., Childs, J. R., Klaeschen, D., Kukowski, N., et al. (1998). New seismic images of the Cascadia subduction zone from cruise SO108 — ORWELL. *Tectonophysics*, *293*(1–2), 69–84. https://doi.org/10.1016/s0040-1951(98)00091-2

Frederiksen, A. W., & Bostock, M. G. (2000). Modelling teleseismic waves in dipping anisotropic structures. *Geophysical Journal International*, *141*(2), 401–412. https://doi.org/10.1046/j.1365-246x.2000.00090.x

Gulick, S. P. S., Meltzer, A. M., & Clarke, S. H. (1998). Seismic structure of the southern Cascadia subduction zone and accretionary prism north of the Mendocino triple junction. *Journal of Geophysical Research*, *103*(B11), 27207–27222. https://doi.org/10.1029/98jb02526

Guo, H., McGuire, J. J., & Zhang, H. (2021). Correlation of porosity variations and rheological transitions on the southern Cascadia megathrust. *Nature Geoscience*, *14*(5), 341–348. https://doi.org/10.1038/s41561-021-00740-1

Gurrola, H., Baker, G. E., & Minster, J. B. (1995). Simultaneous time-domain deconvolution with application to the computation of receiver functions. *Geophysical Journal International*, *120*(3), 537–543. https://doi.org/10.1111/j.1365-246x.1995.tb01837.x

Han, S., Carbotte, S. M., Canales, J. P., Nedimović, M. R., Carton, H., Gibson, J. C., & Horning, G. W. (2016). Seismic reflection imaging of the Juan de Fuca plate from ridge to trench: New constraints on the distribution of faulting and evolution of the crust prior to subduction. *Journal of Geophysical Research: Solid Earth*, *121*(3), 1849–1872. https://doi.org/10.1002/2015jb012416

Hansen, R. T., Bostock, M. G., & Christensen, N. I. (2012). Nature of the low velocity zone in Cascadia from receiver function waveform inversion. *Earth and Planetary Science Letters*, *337–338*, 25–38. https://doi.org/10.1016/j.epsl.2012.05.031

Harris, C. R., Millman, K. J., van der Walt, S. J., Gommers, R., Virtanen, P., Cournapeau, D., et al. (2020). Array programming with NumPy. *Nature*, *585*(7825), 357–362. https://doi.org/10.1038/s41586-020-2649-2

Hayes, G. P., Moore, G. L., Portner, D. E., Hearne, M., Flamme, H., Furtney, M., & Smoczyk, G. M. (2018). Slab2, a comprehensive subduction zone geometry model. *Science*, *362*(6410), 58–61. https://doi.org/10.1126/science.aat4723

Hunter, J. D. (2007). Matplotlib: A 2D graphics environment. *Computing in Science & Engineering*, *9*(3), 90–95. https://doi.org/10.1109/MCSE.2007.55

Ichinose, G. A., Thio, H. K., & Somerville, P. G. (2004). Rupture process and near-source shaking of the 1965 Seattle-Tacoma and 2001 Nisqually, intraslab earthquakes. *Geophysical Research Letters*, *31*(10), L10604. https://doi.org/10.1029/2004gl019668

International Seismological Centre. (2023). ISC-GEM earthquake catalogue [Dataset]. International Seismological Centre. https://doi.org/10.31905/d808b825

IRIS Transportable Array. (2003). USArray transportable array [Dataset]. International Federation of Digital Seismograph Networks. https://doi.org/10.7914/SN/TA

Kan, L.-Y., Chevrot, S., & Monteiller, V. (2023). Dehydration of the subducting Juan de Fuca plate and fluid pathways revealed by full waveform inversion of teleseismic P and SH waves in central Oregon. *Journal of Geophysical Research: Solid Earth*, *128*(4), e2022JB025506. https://doi.org/10.1029/2022jb025506

Kao, H., Shan, S.-J., Dragert, H., Rogers, G., Cassidy, J. F., & Ramachandran, K. (2005). A wide depth distribution of seismic tremors along the northern Cascadia margin. *Nature*, *436*(7052), 841–844. https://doi.org/10.1038/nature03903

Kao, H., Wang, K., Chen, R.-Y., Wada, I., He, J., & Malone, S. D. (2008). Identifying the rupture plane of the 2001 Nisqually, Washington, earthquake. *Bulletin of the Seismological Society of America*, *98*(3), 1546–1558. https://doi.org/10.1785/0120070160

Kao, H., Wang, K., Dragert, H., Kao, J. Y., & Rogers, G. (2010). Estimating seismic moment magnitude (Mw) of tremor bursts in northern Cascadia: Implications for the "seismic efficiency" of episodic tremor and slip. *Geophysical Research Letters*, *37*(19), L19306. https://doi.org/10.1029/2010gl044927

Keach, R. W., Oliver, J. E., Brown, L. D., & Kaufman, S. (1989). Cenozoic active margin and shallow cascades structure: COCORP results from western Oregon. *Geological Society of America Bulletin*, *101*(6), 783–794. https://doi.org/10.1130/0016-7606(1989)101⟨0783:camasc⟩2.3.co;2

Kennett, B. L. N. (1991). The removal of free surface interactions from three-component seismograms. *Geophysical Journal International*, *104*(1), 153–154. https://doi.org/10.1111/j.1365-246x.1991.tb02501.x

Kirkpatrick, S., Gelatt, C. D., & Vecchi, M. P. (1983). Optimization by simulated annealing. *Science*, *220*(4598), 671–680. https://doi.org/10.1126/science.220.4598.671

Krischer, L., Megies, T., Barsch, R., Beyreuther, M., Lecocq, T., Caudron, C., & Wassermann, J. (2015). ObsPy: A bridge for seismology into the scientific Python ecosystem. *Computational Science & Discovery*, *8*(1), 014003. https://doi.org/10.1088/1749-4699/8/1/014003

Langston, C. A., & Blum, D. E. (1977). The April 29, 1965, Puget sound earthquake and the crustal and upper mantle structure of western Washington. *Bulletin of the Seismological Society of America*, *67*(3), 693–711. https://doi.org/10.1785/bssa0670030693

Levander, A. (2007). Seismic and geodetic investigations of Mendocino triple junction dynamics [Dataset]. International Federation of Digital Seismograph Networks. https://doi.org/10.7914/SN/XQ_2007

Li, X., Sobolev, S., Kind, R., Yuan, X., & Estabrook, C. (2000). A detailed receiver function image of the upper mantle discontinuities in the Japan subduction zone. *Earth and Planetary Science Letters*, *183*(3–4), 527–541. https://doi.org/10.1016/s0012-821x(00)00294-6

Liu, D., Zhao, L., Paul, A., Yuan, H., Solarino, S., Aubert, C., et al. (2022). Receiver function mapping of the mantle transition zone beneath the Western Alps: New constraints on slab subduction and mantle upwelling. *Earth and Planetary Science Letters*, *577*, 117267. https://doi.org/10.1016/j.epsl.2021.117267

Luo, Y., & Liu, Z. (2021). Fault zone heterogeneities explain depth-dependent pattern and evolution of slow earthquakes in Cascadia. *Nature Communications*, *12*(1), 1959. https://doi.org/10.1038/s41467-021-22232-x

MacKay, M. E., Moore, G. F., Cochrane, G. R., Moore, J. C., & Kulm, L. D. (1992). Landward vergence and oblique structural trends in the Oregon margin accretionary prism: Implications and effect on fluid flow. *Earth and Planetary Science Letters*, *109*(3–4), 477–491. https://doi.org/10.1016/0012-821x(92)90108-8

Malone, S., Creager, K., Rondenay, S., Melbourne, T., & Abers, G. (2006). Collaborative research: Earthscope integrated investigations of Cascadia subduction zone tremor, structure and process [Dataset]. International Federation of Digital Seismograph Networks. https://doi.org/10.7914/SN/XU_2006

Mann, M. E., Abers, G. A., Crosbie, K., Creager, K., Ulberg, C., Moran, S., & Rondenay, S. (2019). Imaging subduction beneath Mount St. Helens: Implications for slab dehydration and magma transport. *Geophysical Research Letters*, *46*(6), 3163–3171. https://doi.org/10.1029/2018GL081471

McCrory, P. A., Blair, J. L., Oppenheimer, D. H., & Walter, S. R. (2004). Depth to the Juan de Fuca slab beneath the Cascadia subduction margin–a 3-D model for sorting earthquakes. *US Geological Survey*. https://doi.org/10.3133/ds91

McCrory, P. A., Blair, J. L., Waldhauser, F., & Oppenheimer, D. H. (2012). Juan de Fuca slab geometry and its relation to Wadati-Benioff zone seismicity. *Journal of Geophysical Research*, *117*(B9), B09306. https://doi.org/10.1029/2012jb009407

McGary, R. S., Evans, R. L., Wannamaker, P. E., Elsenbeck, J., & Rondenay, S. (2014). Pathway from subducting slab to surface for melt and fluids beneath Mount Rainier. *Nature*, *511*(7509), 338–340. https://doi.org/10.1038/nature13493

Merrill, R., Bostock, M. G., Peacock, S. M., Calvert, A. J., & Christensen, N. I. (2020). A double difference tomography study of the Washington forearc: Does Siletzia control crustal seismicity? *Journal of Geophysical Research: Solid Earth*, *125*(10), e2020JB019750. https://doi.org/10.1029/2020jb019750

Merrill, R., Bostock, M. G., Peacock, S. M., Schaeffer, A. J., & Roecker, S. W. (2022). Complex structure in the Nootka fault zone revealed by double-difference tomography and a new earthquake catalog. *Geochemistry, Geophysics, Geosystems*, *23*(2), e2021GC010205. https://doi.org/10.1029/2021gc010205

Michailos, K., Hetényi, G., Scarponi, M., Stipčević, J., Bianchi, I., Bonatto, L., et al. (2023). Moho depths beneath the European Alps: A homogeneously processed map and receiver functions database. *Earth System Science Data*, *15*(5), 2117–2138. https://doi.org/10.5194/essd-15-2117-2023

Mitchell, C. E., Vincent, P., Weldon, R. J., & Richards, M. A. (1994). Present-day vertical deformation of the Cascadia margin, Pacific northwest, United States. *Journal of Geophysical Research*, *99*(B6), 12257–12277. https://doi.org/10.1029/94jb00279

Morton, E. A., Bilek, S. L., & Rowe, C. A. (2023). Cascadia subduction zone fault heterogeneities from newly detected small magnitude earthquakes. *Journal of Geophysical Research: Solid Earth*, *128*(6), e2023JB026607. https://doi.org/10.1029/2023jb026607

Nabelek, J., Li, X., Azevedo, S., Braunmiller, J., Fabritius, A., Leitner, B., et al. (1993). A high-resolution image of the Cascadia subduction zone from teleseismic converted phases recorded by a broadband seismic array. *Eos Trans. AGU*, *74*(43), 431.

Natural Resources Canada (NRCAN Canada). (1975). Canadian national seismograph network [Dataset]. International Federation of Digital Seismograph Networks. https://doi.org/10.7914/SN/CN

Nedimović, M. R., Bohnenstiehl, D. R., Carbotte, S. M., Canales, J. P., & Dziak, R. P. (2009). Faulting and hydration of the Juan de Fuca plate system. *Earth and Planetary Science Letters*, *284*(1–2), 94–102. https://doi.org/10.1016/j.epsl.2009.04.013

Nedimović, M. R., Hyndman, R. D., Ramachandran, K., & Spence, G. D. (2003). Reflection signature of seismic and aseismic slip on the northern Cascadia subduction interface. *Nature*, *424*(6947), 416–420. https://doi.org/10.1038/nature01840

Nicholson, T., Bostock, M., & Cassidy, J. F. (2005). New constraints on subduction zone structure in northern Cascadia. *Geophysical Journal International*, *161*(3), 849–859. https://doi.org/10.1111/j.1365-246X.2005.02605.x

Niu, F., Levander, A., Ham, S., & Obayashi, M. (2005). Mapping the subducting Pacific slab beneath southwest Japan with Hi-net receiver functions. *Earth and Planetary Science Letters*, *239*(1–2), 9–17. https://doi.org/10.1016/j.epsl.2005.08.009

Northern California Earthquake Data Center. (2014). Berkeley digital seismic network (BDSN) [Dataset]. Northern California Earthquake Data Center. https://doi.org/10.7932/BDSN

Nuttli, O. W. (1952). The western Washington earthquake of April 13, 1949. *Bulletin of the Seismological Society of America*, *42*(1), 21–28. https://doi.org/10.1785/bssa0420010021

Plourde, A. P., Bostock, M. G., Audet, P., & Thomas, A. M. (2015). Low-frequency earthquakes at the southern Cascadia margin. *Geophysical Research Letters*, *42*(12), 4849–4855. https://doi.org/10.1002/2015gl064363

Riddihough, R. (1984). Recent movements of the Juan de Fuca plate system. *Journal of Geophysical Research*, *89*(B8), 6980–6994. https://doi.org/10.1029/jb089ib08p06980

Rodriguez, E., & Russo, R. (2019). Southern Chile crustal structure from teleseismic receiver functions: Responses to ridge subduction and terrane assembly of Patagonia. *Geosphere*, *16*(1), 378–391. https://doi.org/10.1130/ges01692.1

Rohr, K. M., Furlong, K. P., & Riedel, M. (2018). Initiation of strike-slip faults, serpentinization, and methane: The Nootka fault zone, the Juan de Fuca-explorer plate boundary. *Geochemistry, Geophysics, Geosystems*, *19*(11), 4290–4312. https://doi.org/10.1029/2018gc007851

Rondenay, S., Bostock, M. G., & Shragge, J. (2001). Multiparameter two-dimensional inversion of scattered teleseismic body waves 3. application to the Cascadia 1993 data set. *Journal of Geophysical Research*, *106*(B12), 30795–30807. https://doi.org/10.1029/2000jb000039

Royer, A., & Bostock, M. (2014). A comparative study of low frequency earthquake templates in northern Cascadia. *Earth and Planetary Science Letters*, *402*, 247–256. https://doi.org/10.1016/j.epsl.2013.08.040

Sandwell, D. T. (1987). Biharmonic spline interpolation of GEOS-3 and SEASAT altimeter data. *Geophysical Research Letters*, *14*(2), 139–142. https://doi.org/10.1029/gl014i002p00139

Savard, G., Bostock, M. G., & Christensen, N. I. (2018). Seismicity, metamorphism, and fluid evolution across the northern Cascadia fore arc. *Geochemistry, Geophysics, Geosystems*, *19*(6), 1881–1897. https://doi.org/10.1029/2017gc007417

Savard, G., Bostock, M. G., Hutchinson, J., Kao, H., Christensen, N. I., & Peacock, S. M. (2020). The northern terminus of Cascadia subduction. *Journal of Geophysical Research: Solid Earth*, *125*(6), e2019JB018453. https://doi.org/10.1029/2019jb018453

Singer, J., Kissling, E., Diehl, T., & Hetényi, G. (2017). The underthrusting Indian crust and its role in collision dynamics of the Eastern Himalaya in Bhutan: Insights from receiver function imaging. *Journal of Geophysical Research: Solid Earth*, *122*(2), 1152–1178. https://doi.org/10.1002/2016jb013337

Song, T.-R. A., Helmberger, D. V., Brudzinski, M. R., Clayton, R. W., Davis, P., Pérez-Campos, X., & Singh, S. K. (2009). Subducting slab ultra-slow velocity layer coincident with silent earthquakes in southern Mexico. *Science*, *324*(5926), 502–506. https://doi.org/10.1126/science.1167595

Subedi, S., Hetényi, G., Vergne, J., Bollinger, L., Lyon-Caen, H., Farra, V., et al. (2018). Imaging the Moho and the main Himalayan thrust in western Nepal with receiver functions. *Geophysical Research Letters*, *45*(24), 13222–13230. https://doi.org/10.1029/2018gl080911

Tauzin, B., Bodin, T., Debayle, E., Perrillat, J.-P., & Reynard, B. (2016). Multi-mode conversion imaging of the subducted Gorda and Juan de Fuca plates below the North American continent. *Earth and Planetary Science Letters*, *440*, 135–146. https://doi.org/10.1016/j.epsl.2016.01.036

Tréhu, A. M., & Williams, M. (2008). Central Oregon locked zone array, monitoring seismicity associated with a possible asperity on the Cascadia megathrust [Dataset]. International Federation of Digital Seismograph Networks. https://doi.org/10.7914/SN/XA_2008

Tréhu, A. M., Asudeh, I., Brocher, T. M., Luetgert, J. H., Mooney, W. D., Nabelek, J. L., & Nakamura, Y. (1994). Crustal architecture of the Cascadia forearc. *Science*, *266*(5183), 237–243. https://doi.org/10.1126/science.266.5183.237

Tréhu, A. M., Blakely, R. J., & Williams, M. C. (2012). Subducted seamounts and recent earthquakes beneath the central Cascadia forearc. *Geology*, *40*(2), 103–106. https://doi.org/10.1130/g32460.1

Uieda, L., Tian, D., Leong, W. J., Schlitzer, W., Grund, M., Jones, M., et al. (2023). PyGMT: A Python interface for the generic mapping tools [Software]. Zenodo. https://doi.org/10.5281/zenodo.7772533

University of Oregon. (1990). Pacific northwest seismic network - University of Oregon [Dataset]. International Federation of Digital Seismograph Networks. https://doi.org/10.7914/SN/UO

University of Washington. (1963). Pacific northwest seismic network - University of Washington [Dataset]. International Federation of Digital Seismograph Networks. https://doi.org/10.7914/SN/UW

USGS Menlo Park. (1966). USGS Northern California seismic network [Dataset]. International Federation of Digital Seismograph Networks. https://doi.org/10.7914/SN/NC

Virtanen, P., Gommers, R., Oliphant, T. E., Haberland, M., Reddy, T., Cournapeau, D., et al. (2020). SciPy 1.0: Fundamental algorithms for scientific computing in Python. *Nature Methods*, *17*(3), 261–272. https://doi.org/10.1038/s41592-019-0686-2

Waldhauser, F. (2009). Near-real-time double-difference event location using long-term seismic archives, with application to northern California. *Bulletin of the Seismological Society of America*, *99*(5), 2736–2748. https://doi.org/10.1785/0120080294

Wang, K., & Rogers, G. C. (1994). An explanation for the double seismic layers north of the Mendocino triple junction. *Geophysical Research Letters*, *21*(2), 121–124. https://doi.org/10.1029/93gl03538

Watt, J. T., & Brothers, D. S. (2020). Systematic characterization of morphotectonic variability along the Cascadia convergent margin: Implications for shallow megathrust behavior and tsunami hazards. *Geosphere*, *17*(1), 95–117. https://doi.org/10.1130/ges02178.1

Wech, A. G. (2010). Interactive tremor monitoring. [Dataset]. Seismological Research Letters, *81*(4), 664–669. https://doi.org/10.1785/gssrl.81.4.664

Wech, A. G., & Creager, K. C. (2011). A continuum of stress, strength and slip in the Cascadia subduction zone. *Nature Geoscience*, *4*(9), 624–628. https://doi.org/10.1038/ngeo1215

Wells, R., Bukry, D., Friedman, R., Pyle, D., Duncan, R., Haeussler, P., & Wooden, J. (2014). Geologic history of Siletzia, a large igneous province in the Oregon and Washington coast range: Correlation to the geomagnetic polarity time scale and implications for a long-lived yellowstone hotspot. *Geosphere*, *10*(4), 692–719. https://doi.org/10.1130/ges01018.1

Wells, R., Weaver, C. S., & Blakely, R. J. (1998). Fore-arc migration in Cascadia and its neotectonic significance. *Geology*, *26*(8), 759. https://doi.org/10.1130/0091-7613(1998)026⟨0759:famica⟩2.3.co;2

Wessel, P., & Becker, J. M. (2008). Interpolation using a generalized Green's function for a spherical surface spline in tension. *Geophysical Journal International*, *174*(1), 21–28. https://doi.org/10.1111/j.1365-246x.2008.03829.x

Wessel, P., Luis, J. F., Uieda, L., Scharroo, R., Wobbe, F., Smith, W. H. F., & Tian, D. (2019). The Generic Mapping Tools version 6. *Geochemistry, Geophysics, Geosystems*, *20*(11), 5556–5564. https://doi.org/10.1029/2019gc008515

Wilson, D. S. (1989). Deformation of the so-called Gorda plate. *Journal of Geophysical Research*, *94*(B3), 3065–3075. https://doi.org/10.1029/jb094ib03p03065

Wilson, D. S. (1993). Confidence intervals for motion and deformation of the Juan de Fuca plate. *Journal of Geophysical Research*, *98*(B9), 16053–16071. https://doi.org/10.1029/93jb01227

Xiang, Y., Sun, D., Fan, W., & Gong, X. (1997). Generalized simulated annealing algorithm and its application to the Thomson model. *Physics Letters A*, *233*(3), 216–220. https://doi.org/10.1016/s0375-9601(97)00474-x

Xu, Q., Zhao, J., Yuan, X., Liu, H., Ju, C., Schurr, B., & Bloch, W. (2021). Deep crustal contact between the Pamir and Tarim basin deduced from receiver functions. *Geophysical Research Letters*, *48*(9), e2021GL093271. https://doi.org/10.1029/2021gl093271

Yuan, X., Sobolev, S. V., Kind, R., Oncken, O., Bock, G., Asch, G., et al. (2000). Subduction and collision processes in the Central Andes constrained by converted seismic phases. *Nature*, *408*(6815), 958–961. https://doi.org/10.1038/35050073